

PROJECT ADMINISTRATION DATA SHEET

Project No. G-41-665 (SUBPROJECT) ☒ ORIGINAL ☐ REVISION NO. 10/5/84  
 Project Director: DR UZI LANDMAN GTRI/ PHYSICS  
 Sponsor: Philips Laboratories, 345 Scarborough Road,  
Briarcliff Manor, N.Y. 10510  
 Type Agreement: GTRI Research Agreement B10-640  
 Award Period: From 6-12-84 To 6-11-85 (Performance) 6-11-85 (Reports)  
 Sponsor Amount: 12-81-84 This Change 1-31-87 Total to Date  
 Estimated: \$                      \$ 39,170 (see below)  
 Funded: \$                       
 Cost Sharing Amount: \$ None Cost Sharing No:                       
 Title: Molecular Dynamics of Epitaxial Growth

ADMINISTRATIVE DATA

1) Sponsor Technical Contact:

Dr Emil Arnold  
Philips Laboratories  
(above address)

OCA Contact

2) Sponsor Admin/Contractual Matters:

Mr Lawrence Miller  
Philips Laboratories  
(above address)

Defense Priority Rating: N/A

Military Security Classification: N/A

(or) Company/Industrial Proprietary: YES - SEE BEL

RESTRICTIONS

See Attached                      Supplemental Information Sheet for Additional Requirements.

Travel: Foreign travel must have prior approval - Contact OCA in each case. Domestic travel requires sponsor approval where total will exceed greater of \$500 or 125% of approved proposal budget category.

Equipment: Title vests with GIT

COMMENTS:

Above funded amount includes data rights fee of \$35,000.  
A number of restrictions related to advertising, publications,  
patents, and data rights apply. Reference appropriate  
clauses in the Research Agreement.

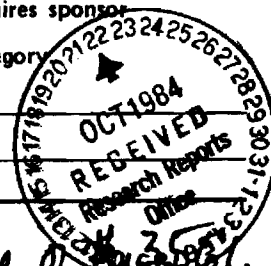
COPIES TO:

Project Director  
 Research Administrative Network OK  
 Research Property Management PRY  
 Accounting

Procurement/EES Supply Services  
 Research Security Services  
Reports Coordinator (OCA)  
 Research Communications (2)

GTRI  
 Library  
 Project File  
 Other                     

Spons ID 02.215,000.84.002



## GEORGIA INSTITUTE OF TECHNOLOGY

## OFFICE OF CONTRACT ADMINISTRATION

SPONSORED PROJECT TERMINATION/CLOSEOUT SHEETDate Sept 23, 1987Project No. G-41-665School/~~Lab~~ PhysicsIncludes Subproject No.(s) N/AProject Director(s) Dr. Uzi LandmanGTRC / ~~GT~~Sponsor Philips LaboratoriesTitle Molecular Epitaxial  
Molecular Dynamics of Epitaxial GrowthEffective Completion Date: 1-31-87

(Performance)

1-31-87

(Reports)

## Grant/Contract Closeout Actions Remaining:

☐ None☒ Final Invoice or Final Fiscal Report☐ Closing Documents☒ Final Report of Inventions Questionnaire sent to P.I.☐ Govt. Property Inventory & Related Certificate☐ Classified Material Certificate☐ Other \_\_\_\_\_

Continues Project No. \_\_\_\_\_

Continued by Project No. \_\_\_\_\_

## COPIES TO:

Project Director  
Research Administrative Network  
Research Property Management  
Accounting  
Procurement/GTRI Supply Services  
Research Security Services  
[REDACTED]  
Legal Services

Library  
GTRC  
Research Communications (2)  
Project File  
Other \_\_\_\_\_

## I. Progress Report

From the initiation of this project we have identified the following as the main issues of theoretical and technological importance in the area of crystal growth from the melt onto an amorphous substrate:

- (a) The structure, stability and dynamics of the equilibrium solid-melt interface (both crystal-melt and amorphous solid-melt interfaces).
- (b) Non-equilibrium phenomena localized to the interface region, which occur during the crystal growth process.
- (c) Phenomena related to crystal face anisotropy.
- (d) Effects due to differences in properties of the amorphous substrate and grown crystal (structural parameters, thermal response).
- (e) The role of impurities in defect stabilization.
- (f) Identification and determination of materials and processing parameters which could be varied in order to achieve desired grown crystal specifications.

Our investigations of the above problems employ molecular dynamics simulations in which the evolution of the system is followed, on refined temporal and spatial scales, via numerical integration of the equations of motions for a large set of interacting particles. This method allows us to perform detailed investigations of the structural and dynamical properties of the system under equilibrium as well as non-equilibrium conditions.

The main issues involved in setting up and in critical assessment of simulation studies are: (i) the faithfulness of the simulated model, focusing mainly on our knowledge of the interaction potentials, and on the ability to employ the appropriately chosen potentials in an economically feasible computational algorithm, (ii) the spatial dimension of the simulated system, and (iii) the finite time span of the simulation.

All the above issues were of particular concern to us since silicon is a

covalently bonded semiconductor, and thus it's directional bonding required us to consider potentials beyond the simple pair-interactions customarily used. In the first stage of our research we have identified appropriate two- and three-body potentials and have developed the first molecular dynamics programs using three-body potentials which in addition incorporated dynamical fluctuations of the volume of the system (i.e., constant pressure simulations). During the past year we have used these molecular dynamics studies and the associated analysis routines in extensive studies of the structure and dynamics of: (i) equilibrium Si crystal-melt interfaces for the (100) and (111) crystalline orientations, (ii) studies of size effects, (iii) epitaxial crystallization from the melt, onto the (100) and (111) crystalline silicon substrates.

The results of our investigations concerning the equilibrium interfaces were published in a coauthored paper with Dr. Arnold's group which provided a most beautiful experimental verification of the faceted structure of the equilibrium Si(100)-melt interface using techniques developed by them at the Philips Laboratories, (Physical Review Letters 56, 155 (1986), entitled: "Faceting at the Silicon (100) Crystal-Melt Interface: Theory and Experiment"), and in a forthcoming publication in the proceedings of the MRS symposium (Boston, December, 1985). In addition the results were presented in talks given by Philips and Georgia Tech researchers at the MRS Meeting (Boston, 1985) and at the APS Meeting (Las Vegas, 1986). In these studies particular care was paid to achieve a true equilibrium of the system and thus determine the solid-melt coexistence temperature (which is found to be in excellent agreement with the experimental value of  $1410^{\circ}\text{C}$ ), and to investigate the simulated system size effects.

Having obtained the equilibrium interfaces for the (100) and (111)

orientations we have studied epitaxial growth onto the Si-crystalline substrate. We have found that:

(a) At a rate of 20 m/sec, growth onto a (100) substrate results in a perfect crystal exhibiting (111) facets at the terminal crystal-vacuum interface. See Fig. 1.

(b) At that rate, growth onto the (111) substrate results in a crystal containing stacking faults and the region of the solidified sample closest to the vacuum is amorphous. Studies of the (111) crystallization system at slower crystallization rates are in progress. See Fig. 2.

(c) For both systems crystallization did not start until the temperature of the system at the solidification front was quite significantly lower than the melting point. See Figs. 3 and 4.

(d) For the Si(111)-melt system, crystallization proceeded in a non-uniform manner, being interrupted by the production of defects and their self-annealing. No such phenomena was found for the (100) system.

(e) The crystallization front is a three-dimensional region, possessing a layered structure in the melt side, which propagates upon solidification.

In addition to these studies we have begun: (i) investigations of the structure of molten silicon in contact with a structureless wall and with an amorphous  $\text{SiO}_2$  substrate, and (ii) investigations of the structural and dynamical properties and stability of microclusters of silicon atoms (3-100 atoms) using various interaction potential models.

Our studies require intensive usage of supercomputers. We have benefitted from access and generous time allocation to the CRAY Computers at Lawrence Livermore Laboratories.

Progress Report

prepared for the North-American Phillips Corporation

period: July 1, 1986 - December 30, 1986

by: Uzi Landman

School of Physics

Georgia Institute of Technology

Atlanta, Georgia 30332

Progress Report

prepared for the North-American Phillips Corporation

period: July 1, 1986 - December 30, 1986

by: Uzi Landman

School of Physics

Georgia Institute of Technology

Atlanta, Georgia 30332

During this report period we have investigated intensively, the mechanisms of solidification of silicon from the melt under various conditions. In our previous studies we have established the structural and energetic characteristics of the solid-melt interface at equilibrium coexistence, which exhibited a faceted structure for the (001) Si crystal-melt interface as opposed to a flat more abrupt interface for the (111) crystalline orientation. In addition to their physical significance, these studies were the first to employ 3-body interaction potentials in molecular dynamics studies. Having obtained the equilibrium, coexistence systems we have focused our attention on non-equilibrium processes which lead to crystal growth. For the purpose of this discussion it is convenient to distinguish between two modes of solidification: (1) Solidification from a melt in contact with a crystalline substrate and (2) solidification onto a unstructured or a disordered substrate.

#### 1. Solidification onto a crystalline substrate (liquid-phase-epitaxy, LPE)

Starting from the equilibrium solid-melt system ((001) and (111) interface orientations) we have driven the system out of equilibrium by allowing heat conduction to the crystalline substrate. This resulted in the initiation of crystalline processes. For both the (001) and (111) systems solidification started only after the liquid supercooled by  $\sim 150^{\circ}\text{K}$  below the melting point.

For the (001) system crystal growth at a rate of  $\sim 18$  m/sec was observed resulting in a perfect crystal which exhibits a faceted structure at the solid-vacuum interface. The faceted morphology of the solid-melt interface maintains throughout the fast crystalline process.

For the (111) cooling at the same rate as for the (001) system resulted in crystal growth at a rate of  $\sim 14$  m/sec. The resulting crystal contains stacking faults, defective layers and an amorphous region. Cooling at a slower rate resulted in crystal growth at a rate of  $\sim 9$  m/sec and the grown



crystal exhibits a much improved structural quality. The crystallization mode on the (111) surface is characterized by a layer-by-layer growth, accompanied by dynamic self-annealing processes.

## 2. Solidification onto a non-crystalline substrate

We have made various attempts to simulate Si crystal growth onto non-crystalline substrates. These substrates were taken to be either structureless walls or amorphous. We have not observed growth of crystals exhibiting crystalline order in any of these simulations. Instead we obtained disordered materials. Various cooling rates were employed but the result did not change.

It is possible that it may be necessary to employ much slower cooling rates for these systems. It may also be the case that the amorphous substrate which we employed was not sufficiently relaxed, or that silicon does not crystallize onto such substrates. Since the completion of this project we have developed improved methods for the preparation of amorphous silicon using the Stillinger-Weber potentials, which agree with experimental data on amorphous silicon. It will be interesting to repeat our growth simulation employing these substrates. It may also be possible that the presence of an enclosing cap (the melt was enclosed between two solid slabs (substrate and cap) interfered with the crystallization process. Instead of attempting to simulate growth on such structureless substrates it may be a better approach to use silicon-dioxide substrates, since possibly the nature of the interface between Si to this substrate (wetting angle, thermal expansion, lattice mismatch, etc.) is more favorable for the growth of ordered crystals.

# Molecular Dynamics Simulations of Epitaxial Crystal Growth

From the Melt: I. Si(100)

Uzi Landman, W. D. Luedtke, M. W. Ribarsky,

R. N. Barnett and C. L. Cleveland

School of Physics, Georgia Institute of Technology, Atlanta, Ga. 30332

## Abstract

Liquid phase epitaxial growth onto a Si(100) substrate is studied using molecular dynamics simulations. The material is described using two- and three-body interaction potentials which provide a realistic description of crystalline silicon and of the crystal-melt interface. Starting from a system prepared at solid-melt coexistence, it is driven out of equilibrium by allowing the conduction of heat to the underlying substrate. Under these conditions the system initially undercools and subsequently crystallization and growth occurs at an overall rate of 18 m/sec, resulting in a perfect crystal. The faceted morphology of the solid-melt interface, characterized by a predominance of (111) microfacets, maintains throughout the fast crystallization stage. The dynamics of the crystal growth process is investigated with refined spatial and temporal resolution via monitoring of real space particle trajectories and of the evolution of system characteristics such as temperature, potential energy and density profiles.

## 1. Introduction

Understanding the mechanisms, kinetics and dynamics of crystal growth processes and identification of the microscopic material properties and of the macroscopic control parameters, related to the method of growth, which govern the growth processes and quality of the grown crystals, are of fundamental importance from both basic and applied perspectives. These issues, therefore, provide the motivation for extensive experimental and theoretical research efforts of these phenomena.<sup>1-10</sup> Indeed, advances in experimental techniques and improved theoretical methods have led to marked enhancement of our knowledge of crystal growth processes, with a focus on refinements of the temporal and spatial resolution on which these phenomena can be studied. Among the various crystal growth techniques, one of the oldest is growth from the melt, or liquid phase epitaxy (LPE).<sup>11</sup> The advent of fast, pulsed laser annealing techniques,<sup>3-10</sup> opened a new era in crystal growth technology, as well as in the theoretical understanding of the microscopics of melting and solidification processes. Though numerous kinetic models of solidification have been proposed and investigated, the complexity of the problem renders it extremely difficult to formulate and implement detailed, accurate, analytical models. On the other hand these systems are suited for computer modeling, in particular computer simulations, which afford systematic probing of the microscopic structure and dynamics of equilibrium and non-equilibrium liquid-solid interfaces<sup>12-21</sup> and thus of crystal growth processes. Timely advances in experimental studies of fast solidification processes and in computational capabilities, along with improvements in our understanding of the energetics and nature of interactions and bonding of materials and in our ability to model them, provide the motivation for intensive investigations, using computer simulations, of the principles of crystal growth of materials

of technological relevance, semiconductors in particular. Having studied in the past<sup>17</sup> the nature of the equilibrium liquid-solid interface of silicon, using interaction potentials<sup>22</sup> which provide a rather faithful description of this material, we explore in this paper<sup>23</sup> the dynamics of LPE of silicon, i.e., the structure and dynamics of the non-equilibrium interface. Since in LPE two condensed phases (solid and liquid) are interacting with one another, (with the interaction driving a phase-transformation of the liquid) it is important that the dynamical nature of the two phases be incorporated in the theoretical model of the growth process. Molecular-Dynamics Simulations are ideally suited for this situation since the dynamics of all particles of the system is followed throughout the calculation thus allowing for cooperative dynamical effects originating from the condensed phase nature of the system.

As in the case of the equilibrium interface where we discovered<sup>17</sup> (theoretically and experimentally) structural anisotropies (i.e., a faceted (001) interface, as opposed to a flat (111) interface) depending on the orientation of the interface, we find that the rate of crystal growth as well as the quality of grown crystal and the type of defects which develop, depend on the crystallographic orientation and on the rate of heat transfer to the substrate. Starting from an equilibrated system at solid-melt coexistence growth is initiated by driving the system out of the equilibrium state via allowing heat conduction to the substrate at a chosen rate. Crystallization does not start until the temperature at the interface drops, from the initial melting point temperature by about 150K. Once the interface region supercools to this degree ordering and crystallization processes start to occur. The liquid-phase epitaxial growth occurs most rapidly on the (001) surface yielding a perfect single crystal at a growth velocity of ~18 m/sec, while growth on the (111) surface (discussed in the following paper) driven by the

same rate of heat removal as for the (001) system yields an imperfect crystal containing an assortment of defects (stacking faults, single defects and disordered regions), at a growth velocity of  $\sim 14$  m/sec. (As shown in the following paper the perfection of the grown crystal on the (111) surface is markedly improved when the growth rate is slowed down to  $\sim 9$  m/sec.) Additionally, we observe that the morphology of the crystal-melt interface maintains a microfaceted structure similar to that found in the equilibrium state. Furthermore, we find that growth from the melt involves cooperative processes, related to the structure and dynamics of the melt in the vicinity of the growth front, and self-annealing processes, which are responsible for the difference in the crystalline perfection in the (111) system for the two growth rates.

In Section 2 of the paper we describe the model interaction potentials which we employ in our calculations and the method of simulation. Our results for LPE on the (001) surface are described in Section 3, and are discussed in the light of recent observations in Section 4.

## 2. Interaction Potential and Simulation Method

The potential energy of a system of interacting particles can be written in general as a sum of contributions of varying order in the number of particles (one-body, two-body, and higher order terms). Because of the directional, covalent, bonding characteristic of tetrahedral semiconductors, a model of the potential for these materials must go beyond the often-used pair interactions. This is achieved via the inclusion of nonadditive, angle-dependent, contributions which describe three-body and higher order interactions.<sup>22</sup>

In our simulations we have employed optimized two- and three-body potentials,  $V_2$  and  $V_3$ , respectively:

$$v_2(r_{ij}) = A[Br_{ij}^{-P} - 1]g_\beta(r_{ij}) \equiv v_{ij} \quad (1a)$$

$$v_3(\vec{r}_i, \vec{r}_j, \vec{r}_k) = v_{jik} + v_{ijk} + v_{ikj} \quad (1b)$$

$$v_{jik} = \lambda g_\gamma(r_{ij})g_\gamma(r_{ik})[\cos\theta_{jik} + \frac{1}{3}]^2, \quad (1c)$$

where  $r_{ij}$  is the distance between atoms  $i$  and  $j$ , and  $g_\gamma(r) = \exp[\gamma/(r-a)]$  for  $r < a$  and vanishes for  $r \geq a$ . In Eqs. (1)  $r$  is expressed in units of  $\sigma = 0.20951$  nm, the unit of energy is  $\epsilon = 50$  kcal/mole, and that of temperature is  $T = \epsilon/k_B$  (to convert to  $T$  in Kelvins multiply the reduced temperature by  $2.517 \times 10^4$ );  $A = 7.049556277$ ,  $B = 0.6022245584$ ,  $P = 4$ ,  $a = 1.8$ ,  $\lambda = 21$ ,  $\beta = 1$ , and  $\gamma = 1.2$ . The time unit, t.u., is  $\sigma(m/\epsilon)^{1/2} = 7.6634 \times 10^{-14}$  sec. As seen from Eq. (1c) the three-body contribution to the potential energy vanishes for the perfect tetrahedral angle. Therefore, the liquid is characterized by a higher magnitude of  $V_3$  than the solid. These potentials have been shown<sup>22,24</sup> to describe adequately various properties of bulk solid and liquid Si and have been used by us<sup>17</sup> and others<sup>18</sup> previously in studies of the equilibrium interface between (100) and (111) crystalline Si and its melt.

Customarily, molecular dynamics simulations employ a constant volume computational cell which is then repeated in space using periodic boundary conditions. However, in order to allow for situations which involve changes in material density and structure in a dynamical manner it is necessary to regard the vectors defining the calculational cell as dynamical variables, i.e., formulate a non-constant volume molecular dynamics method.<sup>25,12</sup> In our simulations we have adopted the Ansatz Lagrangian formulation<sup>25</sup> which we extended to include three-body interactions.

In the constant external pressure molecular dynamics (MD) formulation the position vectors of the particles inside the calculational cell,  $\vec{r}_i$  ( $i = 1, \dots, N$ ), are rewritten in terms of scaled coordinates

$$\vec{s}_i = (\xi, \eta, \zeta) \text{ with } 0 \leq \xi < 1, 0 \leq \eta < 1, 0 \leq \zeta < 1,$$

$$\vec{r}_i = \vec{a}\xi + \vec{b}\eta + \vec{c}\zeta \quad (2)$$

where  $\vec{a}$ ,  $\vec{b}$  and  $\vec{c}$  are three time dependent vectors which span the calculational cell (an arbitrary parallelepiped). Defining the matrix  $\underline{\underline{H}} \equiv (\vec{a}, \vec{b}, \vec{c})$  whose columns are given by the components of vectors  $\vec{a}$ ,  $\vec{b}$  and  $\vec{c}$ , Eq. (2) is written as

$$\vec{r}_i = \underline{\underline{H}} \vec{s}_i \quad (3)$$

The volume of the calculational cell,  $\Omega$ , is given by  $\det \underline{\underline{H}}$  and the distance between particles  $i$  and  $j$  is given in terms of the metric tensor  $\underline{\underline{G}} = \underline{\underline{H}}^T \underline{\underline{H}}$ , where  $\underline{\underline{H}}^T$  denotes the transpose of  $\underline{\underline{H}}$ , by

$$(\vec{r}_i - \vec{r}_j)^2 = (\vec{s}_i - \vec{s}_j)^T \underline{\underline{G}} (\vec{s}_i - \vec{s}_j) \quad (4)$$

Following Parrinello and Rahman<sup>25</sup> we write the Ansatz Lagrangian

$$L = \frac{1}{2} \sum_i m_i \dot{\vec{s}}_i^T \underline{\underline{G}} \dot{\vec{s}}_i - V - P_{\text{ext}} \Omega + \frac{1}{2} W \text{Tr} \underline{\underline{H}}^T \underline{\underline{H}} \quad (5)$$

where  $m_i$  is the mass of particle  $i$ ,  $W$  is a constant having the dimension of

mass and  $V$  is the total interparticle potential (see Eqs. 1).

$$V = \sum_{i < j} v_2(r_{ij}) + \sum_{i < j < k} v_3(\vec{r}_i, \vec{r}_j, \vec{r}_k) \equiv V_2 + V_3. \quad (6)$$

The equations of motions derived from the above Lagrangian are given by

$$m_i \ddot{\vec{s}}_i = - \sum_j \frac{\partial v_{ij}}{\partial \vec{r}_i} + \sum_j \sum_k \left( \frac{\partial v_{jik}}{\partial \vec{r}_j} - \frac{\partial v_{ijk}}{\partial \vec{r}_i} \right) - m_i (\ddot{\vec{H}}^T)^{-1} \ddot{\vec{G}} \cdot \vec{s}_i, \quad (7a)$$

and

$$\ddot{\vec{H}} = [\ddot{\vec{\pi}} - p_{\text{ext}} \vec{1}] \Omega (\ddot{\vec{H}}^T)^{-1}, \quad (7b)$$

where the stress tensor  $\vec{\pi}$  is given by

$$\Omega \vec{\pi} = \sum_i [m_i \vec{v}_i \vec{v}_i - \frac{1}{2} \sum_j \frac{\partial v_{ij}}{\partial \vec{r}_i} \vec{r}_{ij} + \frac{1}{2} \sum_j \sum_k \left( \frac{\partial v_{jik}}{\partial \vec{r}_j} - \frac{\partial v_{ijk}}{\partial \vec{r}_i} \right) \vec{r}_{ij}], \quad (7c)$$

where

$$\vec{v}_i = \ddot{\vec{H}} \cdot \vec{s}_i. \quad (7d)$$



In the above equations the primed summations indicate that terms where  $i$ ,  $j$  or  $k$  are equal are excluded. Interpreting  $\vec{\pi}$  as the internal stress tensor, it is seen from equation (7b) that the time variation of  $\vec{H}$ , describing the dynamical MD calculational cell, is determined by the imbalance between the externally applied pressure  $P_{\text{ext}}$  and the instantaneous value of the internal stress in the system. The time scale of these variations is determined by the mass parameter  $W$ .

Since we are interested in an interface system possessing a free surface, our simulation system is constructed as a thick slab which is periodically repeated in two directions and is free (i.e., no periodic boundary conditions are imposed) in the third direction. Additionally, the slab is positioned on top of a static crystalline silicon substrate which is set up in the desired crystallographic orientation. In all our simulations we begin with a silicon crystal consisting of  $N_L$  dynamic layers with  $N_p$  particles per layer exposing either the (001) or the (111) face (see the following paper). In simulations for the (001) system the  $Z$  axis was taken to be parallel to the [001] direction and the 2D cell is defined by the [110] and  $[\bar{1}\bar{1}0]$  directions. For this system  $N_L = 28$  and  $N_p = 36$  with 4 static substrate layers (i.e., the total number of dynamic particles was 1008. In the numerical integration of the equations of motion, using a fifth-order predictor-corrector algorithm, we employed an integration time step  $\Delta t = 0.015$  t.u.  $= 1.15 \times 10^{-3}$  psec; with this choice and a frequent updating of the interaction lists (every 8  $\Delta t$ ), the total energy of the system is conserved to at least six significant figures (for a few thousand time-steps).

In each of the cases which we studied the preparation procedure of the system was as follows: (i) the system was set up as a Si crystal in the desired configuration and was equilibrated at a reduced temperature of 0.064

(1593°K). (ii) A heat pulse was applied to the top 1/3 of the system (from the vacuum side) via scaling of the particle velocities in that region to 0.19 (4782°K), and the system was allowed to evolve for  $1.5 \times 10^5$  time steps (~175 psec). During this time the heat deposited via the heat pulse spreads over the whole system, raising its temperature to the melting point ( $T_m = 0.0662 \pm 0.0016$  (1665°K) compared to the experimental melting temperature of silicon,  $T_m = 0.0669 \equiv 1683\text{K}$ ), and melting part of it (see Fig. 1 for evolution of the temperature and the 3-body potential energy vs. time during this stage). Thus, during this stage a system at equilibrium solid-melt coexistence is obtained. The system in this state is the starting point for the growth studies. (iii) The growth studies are performed by cooling at a desired rate (via scaling of velocities) the bottom two layers of the dynamic part of the system (i.e., those nearest to the static substrate). That region is sufficiently far from the solid-melt interface to assure that the perturbation to the dynamics caused by the scaling of velocities does not influence the dynamics at the vicinity of the growth front. From our studies of the equilibrium solid-melt coexistence state we determined (see Fig. 2(b) in Ref. 17 and Fig. 5 of this paper) that the average per particle potential energies in the liquid and solid regions are  $-1.78\epsilon$  and  $-1.93\epsilon$  ( $\epsilon = 50$  kcal/mole) and thus our estimate of the per particle latent heat<sup>26</sup> is  $0.15\epsilon$  (31.4 kJ/mole). We have chosen a cooling rate (by scaling the velocities of particles in the bottom two layers every five time steps) such as to remove at a constant rate an amount of energy which is equal to the latent heat per layer ( $N_p \times 0.15\epsilon$ ) every 6 psec. Clearly this rate can be varied as we have done in our studies of LPE on the (111) surface (see following paper).

In the following section we present our results for Si(100). Our result for growth on Si(111) are described in the following paper.

### 3. Liquid Phase Epitaxy on Si(001)

As we discussed previously<sup>17</sup> the equilibrium crystal-melt interface in the (001) orientation exhibits a pronounced structure, with a tendency for the formation of microfacets established on (111) crystal planes, as demonstrated by the sample of particle trajectories, taken from our previous equilibrium studies,<sup>17</sup> shown in Fig. 2. These trajectories were recorded for 2000  $\Delta t$  and viewed along the  $[\bar{1}10]$  direction (normal to the plane of the figure). The breakup of the interface into alternating (111) and  $(\bar{1}\bar{1}\bar{1})$  crystalline planes is evident. Additionally, the melt region in the vicinity of the interface exhibits a degree of ordering due to the crystalline potential, resulting in a diffuseness of the interface in that region. In extended runs we observed that the morphology of the interface fluctuates (on a time scale of  $\sim 4-5 \times 10^3 \Delta t$ ) between equivalent facet configurations.

Starting from the equilibrated system at solid-melt coexistence (i.e., at  $T_m$ ), the system is driven out of equilibrium by allowing heat conduction to the substrate as described in the previous section. The time evolutions of the temperature, and of the 3-body and 2-body contributions to the potential energy of the system during the growth stage are shown in Fig. 3. As seen from this figure in the first stage (up to  $\sim 25$  psec), the system supercools (i.e., the temperature drops below the initial ( $t = 0$ ) melting point temperature). At this initial stage no crystallization occurs as evident from the absence of trends in  $V_3$  and  $V_2$  and monitoring of the structure in the vicinity of the interface. The absence of noticeable crystallization during the initial cooling stage is demonstrated by the time development of  $V_2$  and  $V_3$  shown in Fig. 3 and the system profiles shown in Fig. 5. The sample particle trajectories recorded (over a time span of 3000  $\Delta t$ ) during the beginning of the cooling stage, ( $\sim 10$  psec) shown in Fig. 4, exhibit the structured nature

of the interface, (in this figure the bottom layer is the 5th crystalline layer).

Detailed probing of the growth processes is provided via inspection of profiles of the particle densities,  $\Delta n/\Delta Z^*$  vs.  $Z^*$  along the [001] direction ( $Z^* = 1 = 18.14 \sigma$ ), and profiles of the per-particle potential energy,  $V_2 + V_3$ , as well as those for the individual two- and three-body contributions, taken at selected times during the simulation. The pronounced maxima in the density profiles and the corresponding minima in the potential energy profiles correspond to the locations of crystalline, or partially crystalline layers. Furthermore, we observe that the variation in the total potential energy,  $V_2 + V_3$  upon crossing from the solid to the melt regions, is much smaller than the variation in the individual contributions,  $V_2$  and  $V_3$ . We note that the positive contribution due to the 3-body interaction is smaller in solid regions than in the liquid, as discussed before, while the contribution from the 2-body potentials is less negative in the solid than in the liquid which is consistent with the higher coordination number in the liquid. In addition the absence during the simulations of particles in the vapor phase is consistent with the low experimental triple-point pressure of  $\sim 10^{-1}$  Pa.<sup>26</sup> Inspection of the sample profiles at  $t = 0$  and  $t = 22$  psec, shown in Fig. 5 demonstrates that during this time period no noticeable structural development occurred. In particular the solid-melt (diffuse) interface does not advance during the cooling stage but continues to exhibit a diffuse, structured, character.

Profiles of the system temperature (in units of  $\epsilon$ ) versus  $Z^*$  ( $Z^* = 1 \equiv 18.14 \sigma$ ) at selected times during the simulation are displayed in Fig. 6, (the temperature in a region of space containing  $N'$  particles is defined as

$$(3/2)N'k_B T = (1/2m) \sum_{i=1}^{N'} \vec{p}_i \cdot \vec{p}_i). \text{ These profiles were obtained as short-time}$$

averages ( $2 \times 10^3 \Delta t$ ) and therefore they exhibit a certain degree of noise. Due to the dynamical evolution of the system, in particular the expulsion of latent heat which is accompanying ordering and crystallization processes, we are forced to use such short averaging times. Comparison of the temperature profiles before the start of the heat conduction to the substrate ( $t = 0$ ) and toward the end of the initial cooling stage,  $t = 22$  psec, clearly illustrates the overall drop of the temperature throughout the system below the initial average temperature ( $T_m = 0.0662 \pm 0.0016$ , obtained by long-time averaging at the equilibrium state) and the development of a temperature gradient (see  $t = 22$  psec). It is seen that towards the end of the initial cooling stage ( $t = 22$  psec) the temperature of the interface region (see Figs. 3 and 5) drops to  $\leq 0.06$ , i.e., an undercooling of  $\sim 0.006$  (or  $\sim 150^\circ\text{K}$ ). At about  $t = 25$  psec crystallization of the system starts at the solid-melt interface (see Fig. 3).

In Figs. (7-9) we exhibit system profiles at selected times during the growth simulation. Comparison of the profiles shown in Fig. 7 for  $t = 0$  and 30 psec (compare also  $t = 22$  psec in Fig. 5) demonstrates the ordering processes which begin to take place at  $\sim 25$  psec signifying the start of the crystallization stage. The ordering at the interface region at  $t = 30$  psec is evidenced by a drop of  $V_3$  for layers 14-16 and an enhancement in that region of the layered structure in the density profile. From the temperature profile shown in Fig. 6 we find that at that time the temperature at the interface region is below 0.06. Inspection of the evolution of the system during the subsequent 13 sec, shown in Fig. 8, demonstrates the "explosive" nature of the epitaxial crystallization process in this system, once it starts. We observe that the diffuse nature of the interface, characterized by the gradual transition in the potential energy profiles between the crystalline and melt region, maintains during the crystallization process. An added complication

in attempting to locate the interface in the system under study is the structured (microfaceted or rough) nature of the interface. Nevertheless an estimate of the rate of growth can be obtained by following the time development of minima in  $V_3$  (or  $V_2$ ) and features in the density profiles. Following the evolution of the system from  $t = 30$  psec to  $t = 43$  psec we estimate that the crystallization front advanced during this time span by about 2 crystalline layers. Since the layer spacing is about  $1.3\text{\AA}$  we obtain a crystallization rate of  $\sim 20$  m/sec (when the overall growth process is used in these estimates a rate of  $\sim 18$  m/sec is obtained). Additionally we remark that during the fast crystalline growth the temperature at the solidification front remains at or below 0.06.

Since the crystalline-melt interface at equilibrium (see Fig. 2) and during the initial cooling stage (see Fig. 4) exhibits a characteristic microfaceted morphology it is of interest to inquire about the interface morphology, and the time-scale of its variations, during growth. In Fig. 10(a) we show real space particle trajectories in the interface region recorded during the fast growth stage in the time period 51-58 psec (see Fig. 3), viewed from the  $[\bar{1}10]$  direction. The rough nature of the crystalline-melt interface and the prevalence of (111) planes is evident from the figure. Furthermore, in Fig. 10(b) and 10(c) we show contour plots of the per-particle 3-body potential energy, for particles with  $V_3 \leq 0.45 \epsilon$ . (We have found that such contour plots can be used in order to separate solid from liquid-like regions (the shape of the surface contours does not depend strongly on the cutoff value, in the vicinity of  $0.45\epsilon$ ). These contours were obtained as averages for the time intervals 50.5-51.5 psec (b) and 55.5-56.5 psec (c). These potential contours complement and corroborate the picture of the interface morphology. In addition, since the time period separating the two

contour plots in Figs. 10(b) and 10(c) corresponds roughly to the time that it takes for the crystalline phase to advance by one layer spacing, it gives an idea about the structural and temporal characteristics of the microscopic changes in the interface morphology during growth. To complete the characterization of the system at this stage of growth we display in Fig. 11 the system profiles at  $t = 55$  psec.

In Fig. 9 we show the system profiles at the final stages of the growth process (115 psec, see also Fig. 3), and close to the end of the simulation (160 psec). As seen from the figure, at  $t = 115$  psec most of the system has crystallized and the temperature dropped to below 0.055 (see Fig. 6). The final stages of the process involve structural refinement in the crystalline-vacuum interface region (see  $t = 160$  psec in Fig. 9). The final surface morphology of the grown crystal is shown in Fig. 12, exhibiting a faceted structure with a tendency to expose (111) and  $\overline{(111)}$  planes. The grown crystal possesses a high degree of structural perfection with no registry or intralayer defects.

#### 4. Discussion

Laser annealing techniques, i.e., the heating of a solid by high-power laser irradiation, offer novel methods for the preparation of materials and open new avenues in crystal growth studies by allowing heating and cooling of the surface region of well characterized materials with rates (and to temperatures) which are not attainable by other methods. It is now well accepted that the fast dissipation of the absorbed laser radiation by semiconductors (Si in particular) results in transient melting which leads to rapid solidification with solidification front velocities in the range of several meters per second. As such the term laser annealing is tantamount to ultra-fast liquid-phase epitaxy, since the mechanisms of solidification which

occur subsequent to melting involve liquid and liquid-solid interface processes. Whereas in laser annealing experiments the melt which is produced can be at a temperature which is above the melting temperature (depending on the laser pulse duration and power) there is ample evidence that at the initial stages cooling to the melting point and below it (particularly in the vicinity of the solidification interface) must occur.<sup>27</sup> Therefore it is pertinent to discuss the results of our studies (where the starting point for the growth simulation is a system at solid-melt equilibrium, i.e., at the melting point) in light of the wealth of information obtained in laser-annealing investigations.<sup>3-10</sup>

Melting and solidification of single-component materials have been phenomenologically formulated using two models:<sup>28</sup> (i) the thermodynamic model<sup>29,30</sup> (ii) the kinetic rate theory model.<sup>31</sup> Although both approaches are similar in many respects, the kinetic model can be better applied to nonequilibrium processes. According to this model an expression can be derived for the velocity of the melt-front propagation in terms of the rate,  $k_f$ , in which atoms leave the liquid and add to the solid, the latent heat of solidification,  $L_c$ , the crystallization temperature,  $T_c$ , the interface temperature,  $T_i$ , and the degree of undercooling at the interface,  $\Delta T_i$ .

$$v = k^f [1 - \exp[-(L_c/k_B T_c) \Delta T_i / T_i]]. \quad (8)$$

While for slow, uniform and small degree of undercooling (a situation for which the theory was originally constructed)  $T_i$  can be taken as the melting point, it is not clear what value it should be assigned under the conditions applying to fast growth in the presence of large  $\Delta T_i$ . Nevertheless, the above phenomenologically derived expression emphasizes the fundamental relationship



between supercooling and the velocity of the phase-transformation (solidification or melting). Considerations of the heat flow in a system undergoing a phase transformation emphasize, in addition, the dependence of the velocity of the interface on the heat gradient in the interface region.<sup>28</sup>

These theoretical models, which are based on a number of simplifying assumptions, motivated vast experimental efforts to measure and correlate growth velocities, undercooling, heat-gradients and thermodynamic properties of systems under laser-annealing growth conditions. These are immensely challenging experiments and although a very large body of information has been accumulated, we cite only one experiment,<sup>32</sup> using transient conductance measurements, where the undercooling at an interface velocity of 6 m/sec has been deduced to be 90K. From experiments<sup>33-35</sup> in which melting followed by solidification or amorphization occurs it was concluded that at a velocity of 15 m/sec (above which growth on Si(001) yields an amorphous solid) the liquid must have a greater undercooling than 250°C. Furthermore, in order to achieve such rapid growth it was estimated<sup>34</sup> that cooling rates in excess of  $10^{11}$  °C/sec are achieved. In addition it was estimated<sup>36</sup> that the spatial gradients at the interface for melt-front velocities between 6-18 m/sec are in the range of  $1.14 - 3.43 \times 10^7$  deg/cm. The values which we obtain from our simulations for the above characteristic growth parameters are: the cooling rate (see end of section 2) which we employed corresponds to  $\sim 2 \times 10^{12}$  °K/sec; the temperature gradient at the start of the crystallization process (see temperature profile at  $t = 30$  psec in Fig. 6) is estimated as  $5-7 \times 10^8$  °K/cm and the average growth velocity, resulting in a perfect grown crystal, is 18 m/sec. These values, which are in general good agreement with those deduced from experimental data and analyses of phenomenological growth models, lend strong support as to the realistic merits of our simulations and the

interaction potentials<sup>22</sup> which were employed.

The growth mode which we observed and analysed emphasizes the dynamical nature of the two interacting phases (solid and melt), the kinetics of ordering processes in the melt in the vicinity of the moving interface<sup>13-15</sup> and the interface morphology. Ample evidence exists, mainly through studies of silicon crystalline growth from the melt onto insulating substrates, and on Si(001) substrates, that the surface of crystalline silicon becomes faceted upon melting and that the solid-melt interface of a growing Si crystal establishes itself on the (111) crystal planes.<sup>37</sup> Furthermore, we have discussed previously<sup>17</sup> (see also Fig. 2) the faceted nature of the equilibrium, solid-melt coexistence Si(001) crystal-melt interface. In the present study we found that the microfaceted structure of the interface maintains even at a high-growth velocity.

Finally, our observation that the crystal grown on the (001) silicon substrate at an average velocity of 18 m/sec is structurally perfect should be contrasted with the results which we obtained for LPE growth on Si(111) where the same rate of cooling resulted in a defective crystal grown at a velocity of 14 m/sec (see following paper). Indeed, the orientational dependence of high speed silicon crystal growth from the melt has been observed experimentally,<sup>41,42</sup> demonstrating clearly that the maximum growth interface velocities for the formation of a defect-free crystal can be ordered in the orientation sequence (001) > (011) > (112) > (111). We focus on these effects and offer further discussion in our following paper where LPE on Si(111) is studied.

Acknowledgement

This work was supported by U. S. Department of Energy under grant No. FG05-86ER45234 and in part by a grant from the North-American Philips Corporation. The computations were performed on the CRAY-XMP at the National Magnetic Fusion Energy Computer Center, Livermore, California.

### References

1. Current Topics in Material Science, Vol. 2, 1976, Crystal Growth and Materials, Eds., E. Kaldis and H. J. Scheel (North-Holland, Amsterdam, 1977).
2. Crystal Growth: A Tutorial Approach, Eds. W. Bardsley, D. T. J. Hurle and J. B. Mullin (North-Holland, Amsterdam, 1979).
3. Laser-Solid Interactions and Laser Processing - 1978, AIP Conference Proc. No. 50, Eds., S. D. Ferris, H. J. Leamy and J. M. Poate, (AIP, New York, 1979).
4. Laser and Electron-Beam Interactions with Solids, Eds., B. R. Appleton and G. K. Celler, (North-Holland, Amsterdam, 1982).
5. Laser-Solid Interactions and Transient Thermal Processing of Materials, Eds., J. Narayan, W. L. Brown and R. A. Lemons, (North-Holland, Amsterdam, 1983).
6. Energy Pulse Modifications of Semiconductors and Related Materials (Vols. 1 and 2), Eds., K. Hennig, (Akad. der Wissenschaften der DDR, Rossendorf, 1984).
7. Laser Annealing of Semiconductors, Eds., J. M. Poate and J. W. Mayer (Academic Press, New York, 1982).
8. Semiconductors and Semimetals, Vol. 23: Pulsed Laser Processing of Semiconductors, Eds., R. F. Wood, C. W. White and R. T. Young, (Academic Press, Orlando, 1984).
9. See review by K. A. Jackson in: Surface Modification and Alloying, Eds., J. M. Poate, G. Foti and D. C. Jacobson (Plenum, New York, 1983) Ch. 3.
10. See review by J. M. Poate, J. Cryst. Growth 79, 549 (1986).
11. See review by : J. C. Brice in Ref. 1, p. 571.
12. See references in a review by F. F. Abraham, J. Vac. Sci. Technol. B2,

- 534 (1984); See articles in Fluid Interfacial Phenomena, Ed., C. A. Croxton (Wiley, Chichester, 1986); U. Landman, R. N. Barnett, C. L. Cleveland, W. D. Luedtke, M. W. Ribarsky, D. Scharf and J. Jortner, Mat. Res. Soc. Symp. Proc. 63, 273 (1985).
13. U. Landman, C. L. Cleveland and C. S. Brown, Phys. Rev. Lett. 45, 2032 (1980); U. Landman, C. L. Cleveland, C. S. Brown and R. N. Barnett in Nonlinear Phenomena of Phase Transitions and Instabilities, Ed. T. Riste (Plenum, N. Y., 1982), p. 379.
  14. C. L. Cleveland, U. Landman and R. N. Barnett, Phys. Rev. Lett. 49, 790 (1982).
  15. U. Landman, R. N. Barnett, C. L. Cleveland and R. H. Rast, J. Vac. Sci. Technol. A3, 1574 (1985).
  16. J. Q. Broughton, G. H. Gilmer and K. A. Jackson, Phys. Rev. Lett. 49, 1996 (1982).
  17. U. Landman, W. D. Luedtke, R. N. Barnett, C. L. Cleveland, M. W. Ribarsky, E. Arnold, S. Ramesh, H. Baumgart, A. Martinez and B. Khan, Phys. Rev. Lett. 56, 155 (1986).
  18. F. F. Abraham and J. Q. Broughton, Phys. Rev. Lett. 56, 734 (1986).
  19. R. F. Wood and G. E. Giles, Phys. Rev. B23, 2923 (1981); R. F. Wood, J. R. Kirkpatrick and G. E. Giles, Phys. Rev. B23, 555 (1981); R. F. Wood and G. A. Geist, Phys. Rev. Lett. 57, 873 (1986); see also articles in Ref. 8.
  20. M. O. Thompson and G. J. Calvin in Ref. 5, p. 57.
  21. P. Baeri, S. U. Campisano, G. Foti and E. Rimini, Appl. Phys. Lett. 33, 137 (1978); ibid. 50, 788 (1979); Chapter 4 in Ref. 7.
  22. F. H. Stillinger and T. A. Weber, Phys. Rev. B31, 5262 (1985).
  23. A preliminary report of this work was given in APS Bull. 31, (3), 319 (1986).
  24. J. Q. Broughton and X. P. Li, Phys. Rev. B35, 9120 (1987).

25. M. Parinello and A. Rahman, Phys. Rev. Lett. 45, 1196 (1980);
26. The experimental value of the latent heat is 50.7 kJ/mole (compare also the value of 30.3 kJ/mole obtained in Ref. 18); F. Roseburg, Handbook of Electron Tube and Vacuum Techniques (Addison-Wesley, Reading, Mass., 1965).
27. See reviews in Chapters 4 and 5 of Ref. 8; Ref. 10; Chap. 2 in Ref. 7 and the references cited therein.
28. See review in chapter of Ref. 8.
29. D. Turnbull, Solid State Phys. 3, 225 (1956).
30. See F. Spapen and D. Turnbull in Ref. 7, p. 15.
31. B. Charlmers, Trans. AIME 200, 519 (1954); K. A. Jackson and B. Charlmers, Can. J. Phys. 34, 473 (1956).
32. P. S. Pearcy and M. O. Thompson in: Energy Beam-Solid Interactions and Transient Thermal Processing, Mater. Res. Soc. Proc. 35, Eds., D. K. Bigelsen, G. Rozgonyi and C. Shank (Materials Research Society, Pittsburgh, 1985), p. 53.
33. P. L. Liu, R. Yen, N. Bloembergen and R. T. Hodgson, Appl. Phys. Letters 34, 864 (1979).
34. R. Tsu, R. T. Hodgson, T. Y. Yan and J. E. E. Baglin, Phys. Rev. Lett. 42, 1358 (1979).
35. M. O. Thompson, J. W. Mayer, A. G. Cullis, H. C. Webber, N. G. Chew, J. M. Poate and D. C. Jacobson, Phys. Rev. Lett. 50, 896 (1983).
36. Chap. 4 in Ref. 8, Table III, p. 218.
37. G. K. Celler, K. A. Jackson, L. E. Trimble, Mc. D. Robinson, and D. J. Lischner, in Energy Beam-Solid Interactions and Transient Thermal Processing, edited by J. C. C. Fan and N. M. Johnson (North-Holland, New York, 1984), p. 409.

38. M. W. Geis, H. J. Smith, B.-Y. Tsaur, J. C. C. Fan, D. J. Silversmith, and R. Mountain, J. Electrochem. Soc. 129, 2813 (1982).
39. K. F. Lee, T. J. Stultz, and J. F. Gibbons, in Semiconductors and Semimetals, edited by R. K. Willardson and A. C. Beer (Academic, New York, 1984), Vol. 17, p. 227.
40. L. Pfeiffer, S. Paine, G. H. Gilmer, W. van Saarloos, and K. W. West, Phys. Rev. Lett. 54, 1944 (1985).
41. J. M. Poate, Mat. Res. Soc. Sym. Proc. 4, 121 (1982).
42. A. G. Cullis, N. G. Chew, H. C. Weber and D. J. Smith, J. Cryst. Growth 68, 624 (1984).

## Figure Captions

Figure 1: Time development of the temperature,  $T$ , in units of  $\epsilon$ , and total 3-body potential energy for the system during the sample preparation stage starting from the application of the heat pulse to the upper third of the system at  $t = 0$ . Time is given in psecs. Note the long times required to achieve equilibration. During this stage part of the system melts and an equilibrium solid-melt coexistence is achieved at the melting point  $T_m = 0.0662 \pm 0.0016$  (1665°K).

Figure 2: Real space particle trajectories, recorded over 2000  $\Delta t$ , at the interface region, taken from our equilibrium studies.<sup>17</sup> The system is viewed along the  $[\bar{1}10]$  direction. Distance is measured in units of  $X^* = Y^* \equiv 10.9\sigma$  and  $Z^* = 1 \equiv 18.14\sigma$ . For the system used in that study the interface starts at about layer 6 as noted in the figure. Note the breakup of the interface into alternating (111) and  $(\bar{1}\bar{1}\bar{1})$  crystalline planes forming micro-facets. The 2D computational cell ( $0 \leq X^*, Y^* \leq 1$ ) is replicated along the  $X^*[\bar{1}10]$  direction to aid in visualization.

Figure 3: Time development of the system temperature,  $T$ , in units of  $\epsilon$  and of the per particle 3-body and 2-body contributions to the potential energy throughout the growth simulation, beginning from the start of the heat extraction at  $t = 0$ . The start of the crystallization stage is noted ( $\sim 25$  psec). Prior to this time the system cools down to below the initial melting point temperature.

Figure 4: Real space particle trajectories at the interface region (starting in crystalline layer 5) recorded for 3000  $\Delta t$ , at  $t = 10$  psec after the beginning of the growth simulation (i.e., during the cooling



stage (see Fig. 3). The system is viewed along the  $[\bar{1}10]$  direction. Distances are measured in units of  $X^* = Y^* = 11\sigma$  and  $Z^* = 18.14\sigma$ . Note that the structured, microfaceted character of the interface maintains during the cooling stage. The 2D computational cell ( $0 \leq X^*, Y^* \leq 1$ ) is replicated along the  $X^*[110]$  direction to aid visualization.

**Figure 5:** Profiles of the particle density,  $\Delta n/\Delta Z^*$ , where  $\Delta n$  is the number of particles with  $Z^*$  coordinates between  $Z^*$  and  $Z^* + \Delta Z^*$ , and profiles of the per particle total potential energy,  $V_2 + V_3$ , and of the 2-body and 3-body contributions versus  $Z^*$  ( $Z^* = 1 \equiv 18.14\sigma$ ), at  $t = 0$  and 22 psec. In the crystalline region, maxima in the density profiles and the corresponding minima in the potential energy profiles occur at the crystalline layer positions. Note the diffuse character of the interface (see also Fig. 4). Comparison of the profiles for the two times demonstrates that no observable crystallization or ordering had occurred during the initial cooling stage.

**Figure 6:** Temperature,  $T$ , profiles of the system at selected times during the simulation. The  $t = 0$  profile was recorded for the equilibrium solid-melt coexistence system prior to the beginning of the growth simulation. All the profiles were obtained as short-time averages over  $2 \times 10^3$  At.

**Figure 7:** Profiles of the system particle density, of the per particle total potential energy  $V_2 + V_3$ , and of the 2-body,  $V_2$ , and 3-body,  $V_3$ , contributions at the start of the growth simulation  $t = 0$ , and shortly after the start of crystallization,  $t = 30$  psec (see Fig. 3). See caption to Fig. 5 for further detail.

Figure 8: Same as Fig. 7 for  $t = 36$  psec and 43 psec, illustrating the evolution of the system during growth.

Figure 9: Same as Fig. 7 for  $t = 115$  psec and 160 psec, at the end of the fast crystallization process and at the final stage of the simulation, respectively.

Figure 10: (a) Real space particle trajectories at the interface region, starting at crystalline layer number 13, recorded during the fast growth stage in the time span 51-58 psec (about the time period for growth of one crystalline layer). The system is viewed along the  $[110]$  direction and length is in the units given in the caption to Fig. 4. The figure demonstrates that the structured character of the interface maintains during the fast crystallization process (compare Figs. 2 and 4). (b) Contour plot of  $V_3$ , recorded at 50.5-51.5 psec, for particles with per particle  $V_3 \leq 0.45 \epsilon$ , exhibiting the morphology of the interface between the solid region of the sample and the melt (which possess per particle  $V_3$  values greater than  $0.45\epsilon$ ). (c) Same as (b), recorded towards the end of the time interval shown in (a), 55.5-56.5 psec. Comparison of (b) and (c) illustrates the manner in which the interface morphology varies during growth of a layer.

Figure 11: Profiles of the system particle density, of the particle total potential energy,  $V_2 + V_3$ , and of the 2-body,  $V_2$ , and 3-body,  $V_3$ , contributions during the fast growth process, at 55 psec.

Figure 12: Real space particle trajectories of the system, starting at crystalline layer 21, at the end of the growth simulation study  $t = 160$  psec, recorded for 3000  $\Delta t$ , demonstrating a structured, microfaceted, crystalline-vacuum interface with a tendency to form

(111) planes. The system is viewed from the [001] direction. The units of length as in Fig. 4. The 2D computational cell ( $0 \leq X^*$ ,  $Y^* \leq 1$ ) was replicated along the  $X^*[110]$  direction to aid visualization.

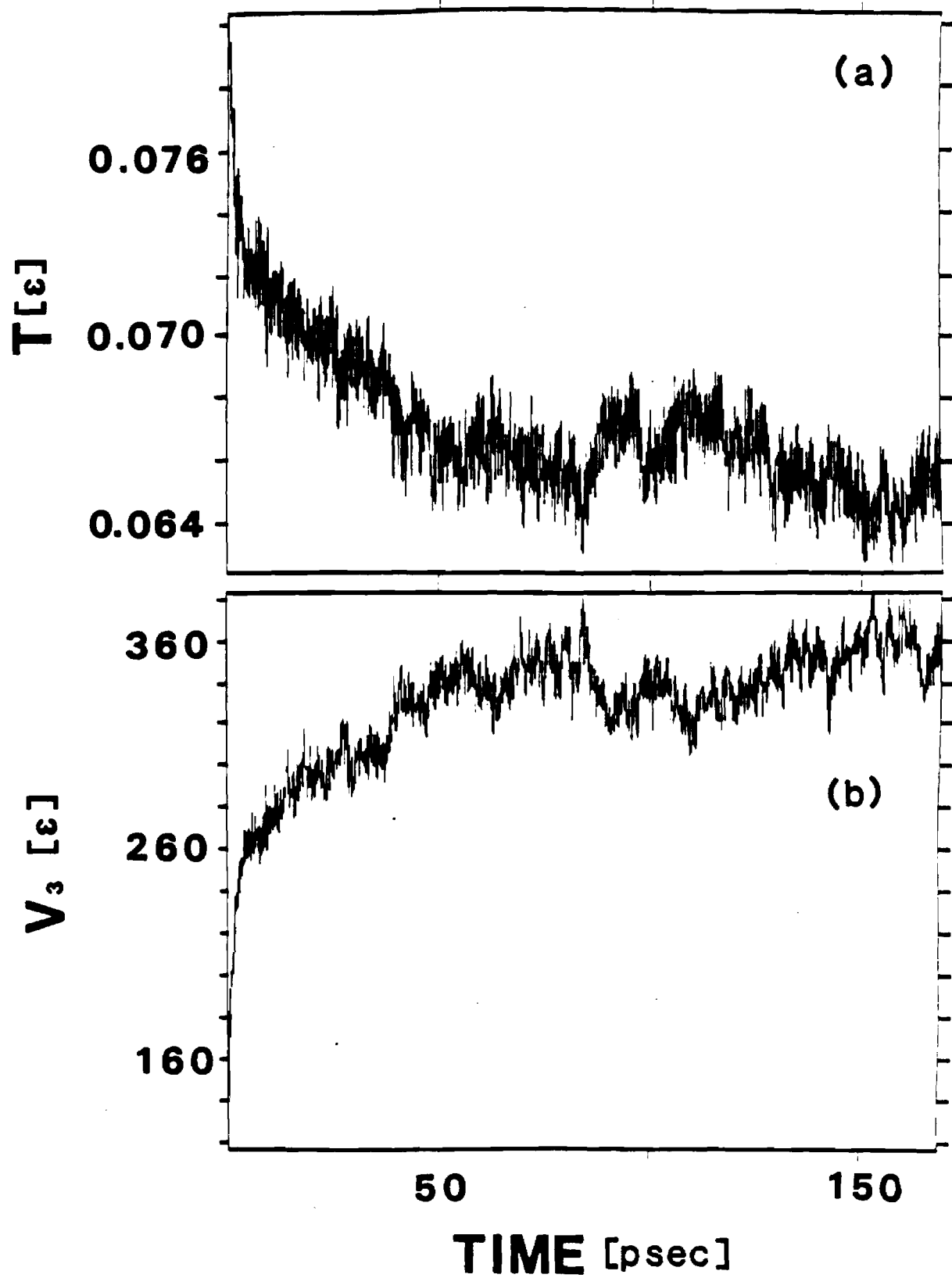


FIGURE 1

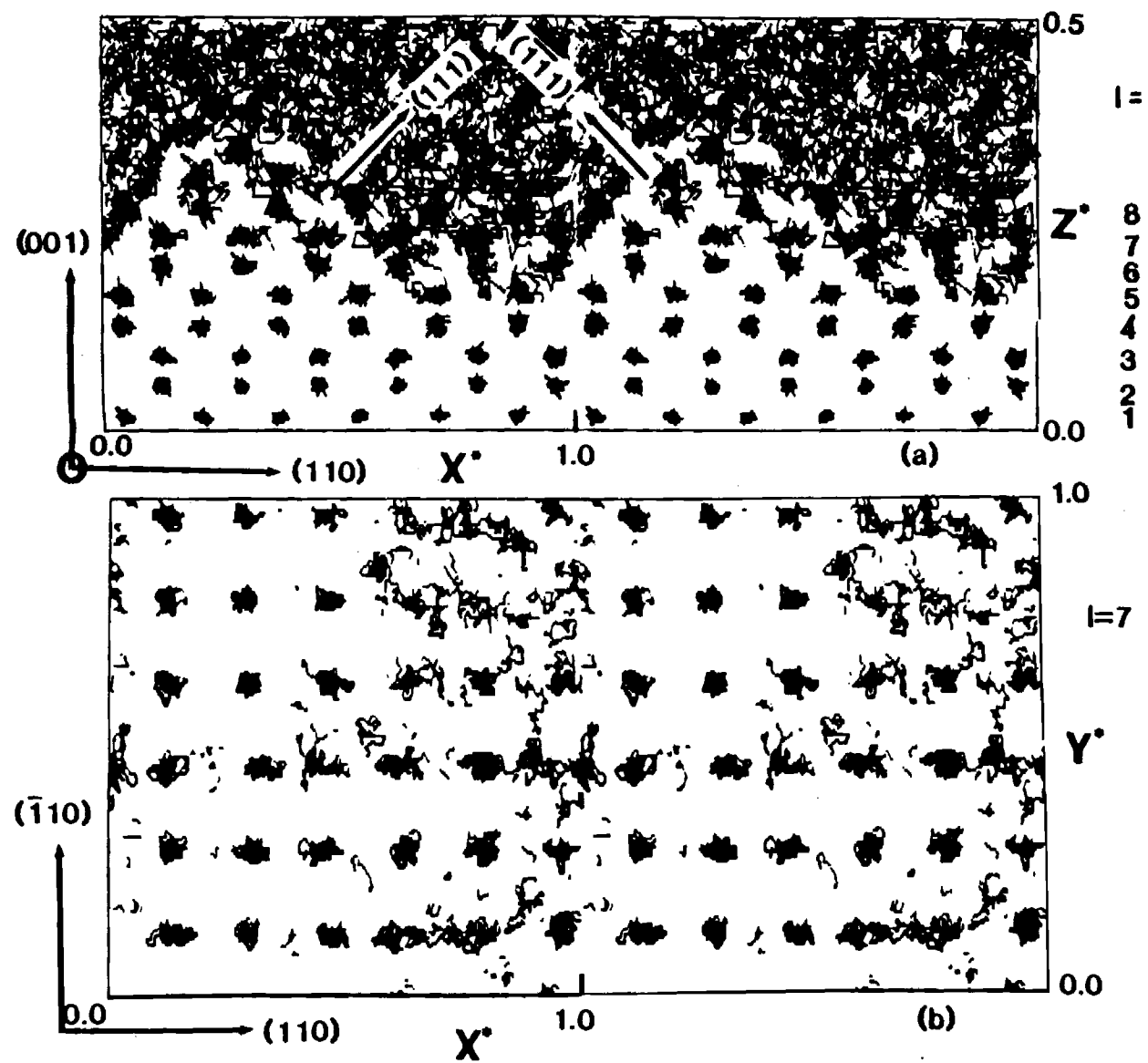


FIGURE 2

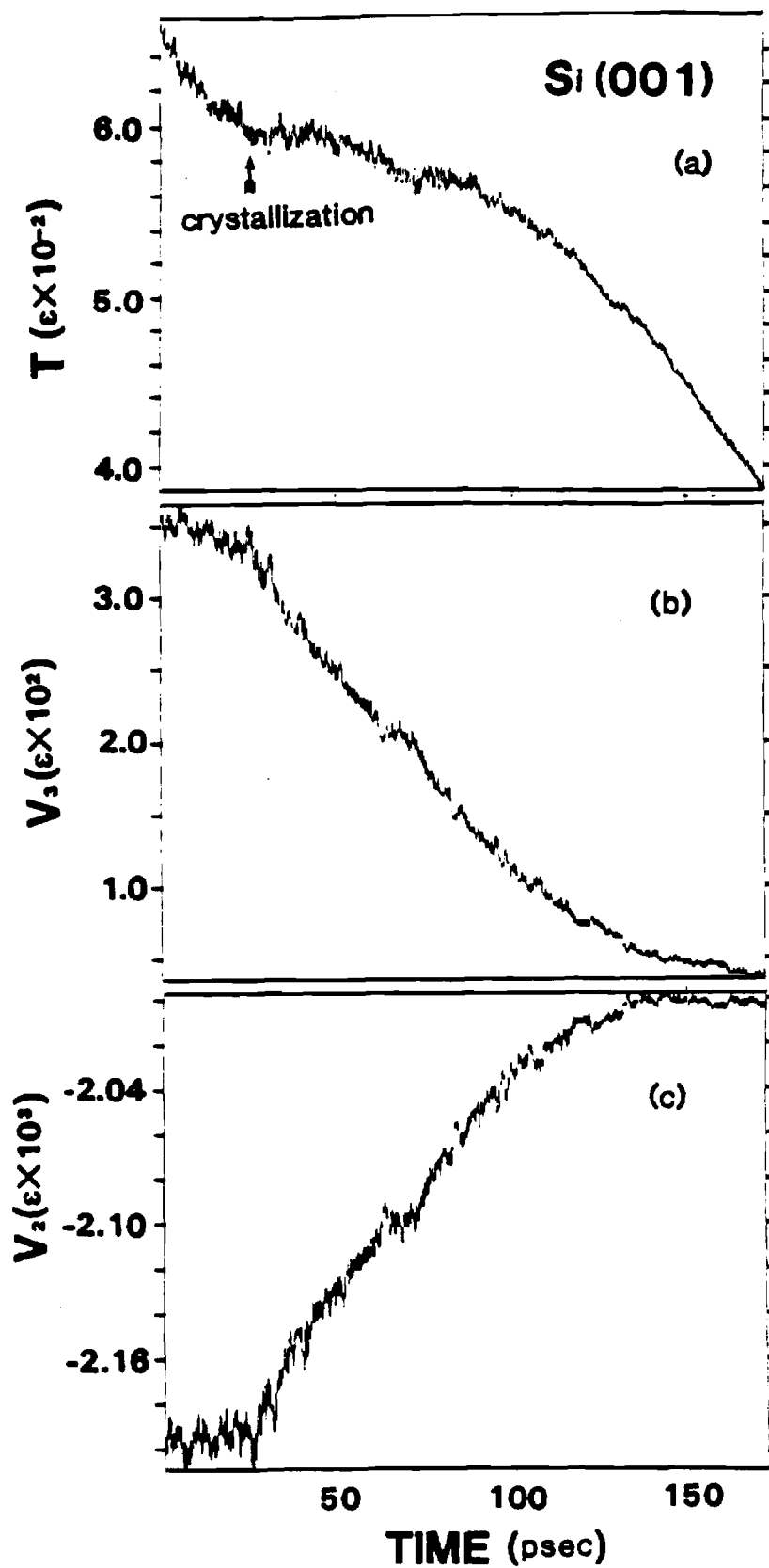


FIGURE 3

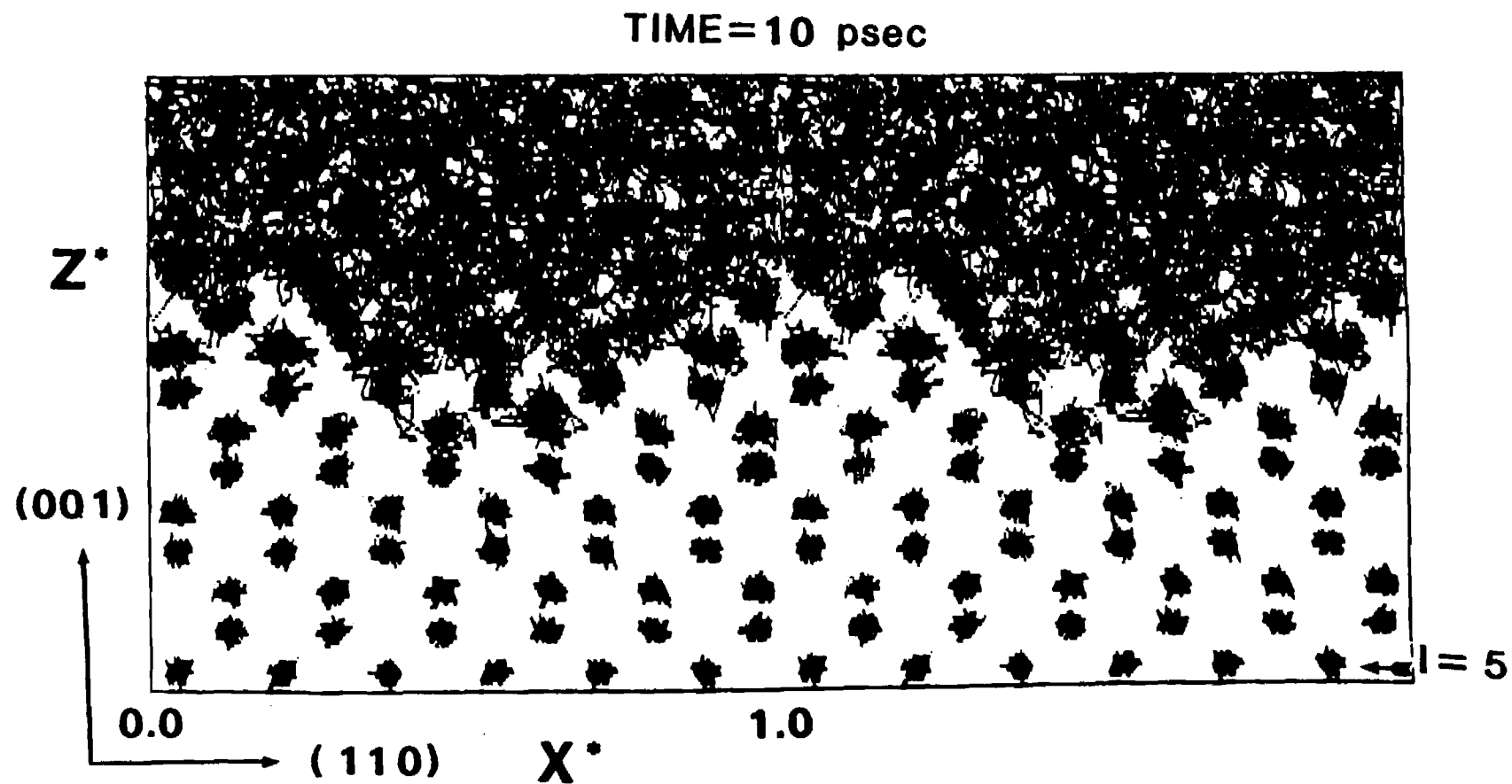


FIGURE 4

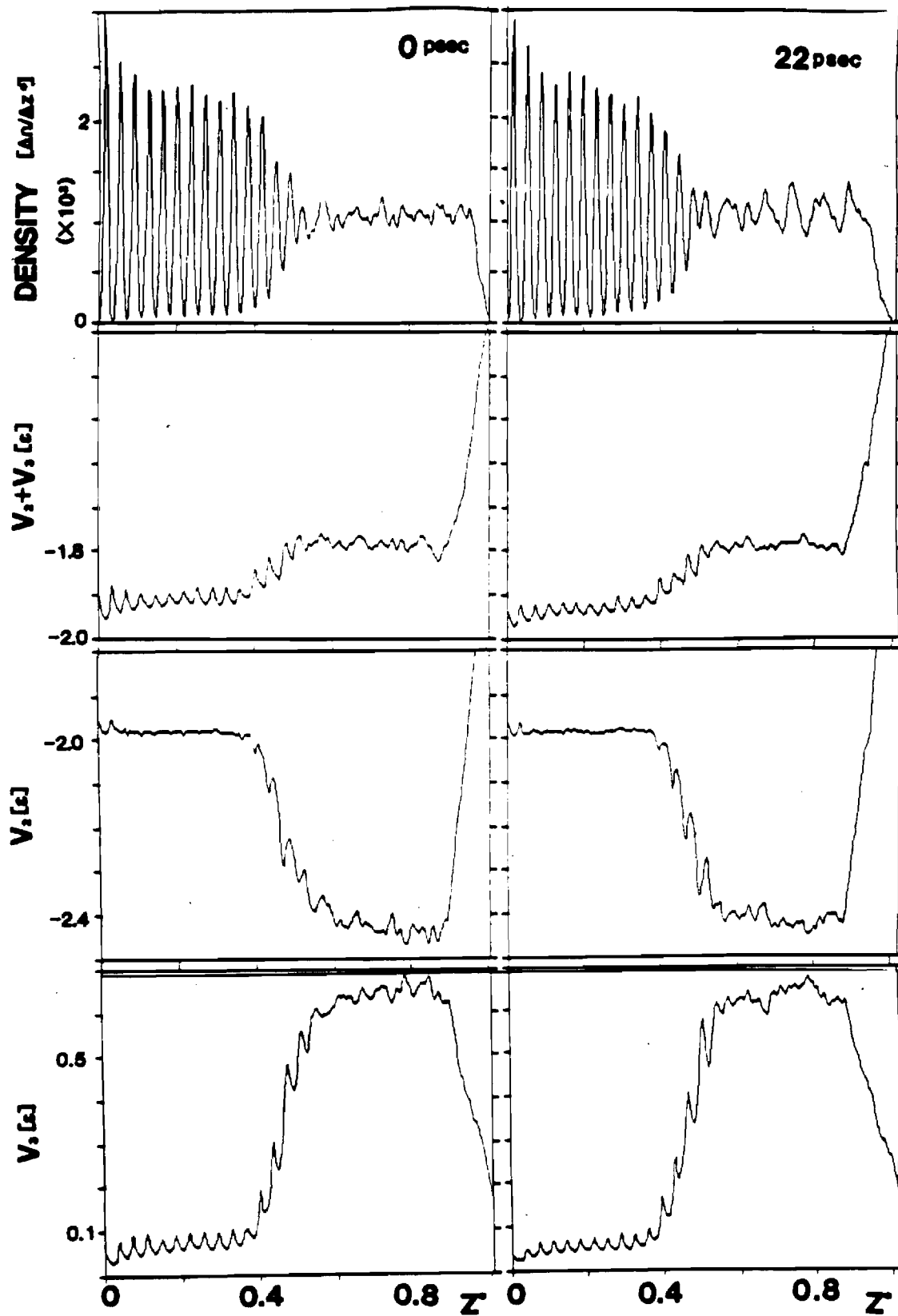


FIGURE 5



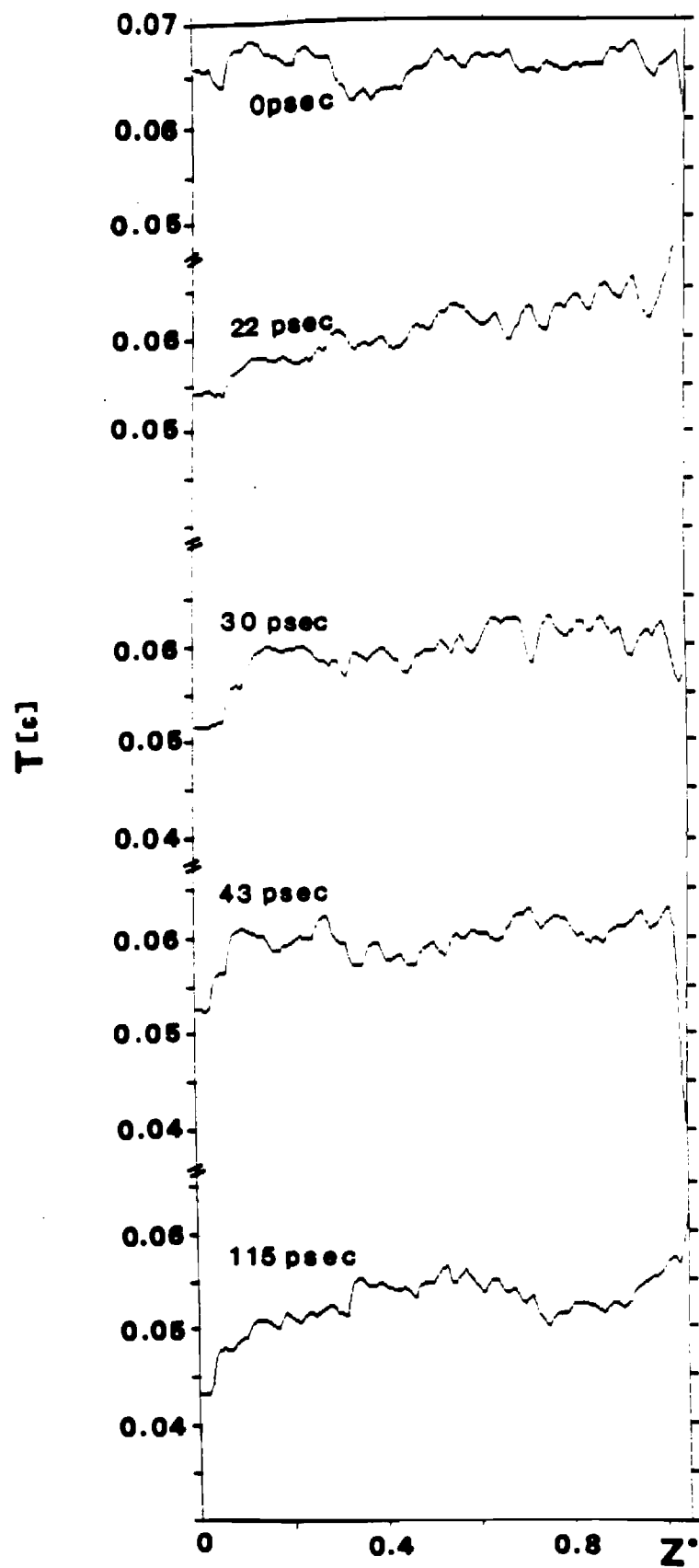


FIGURE 6

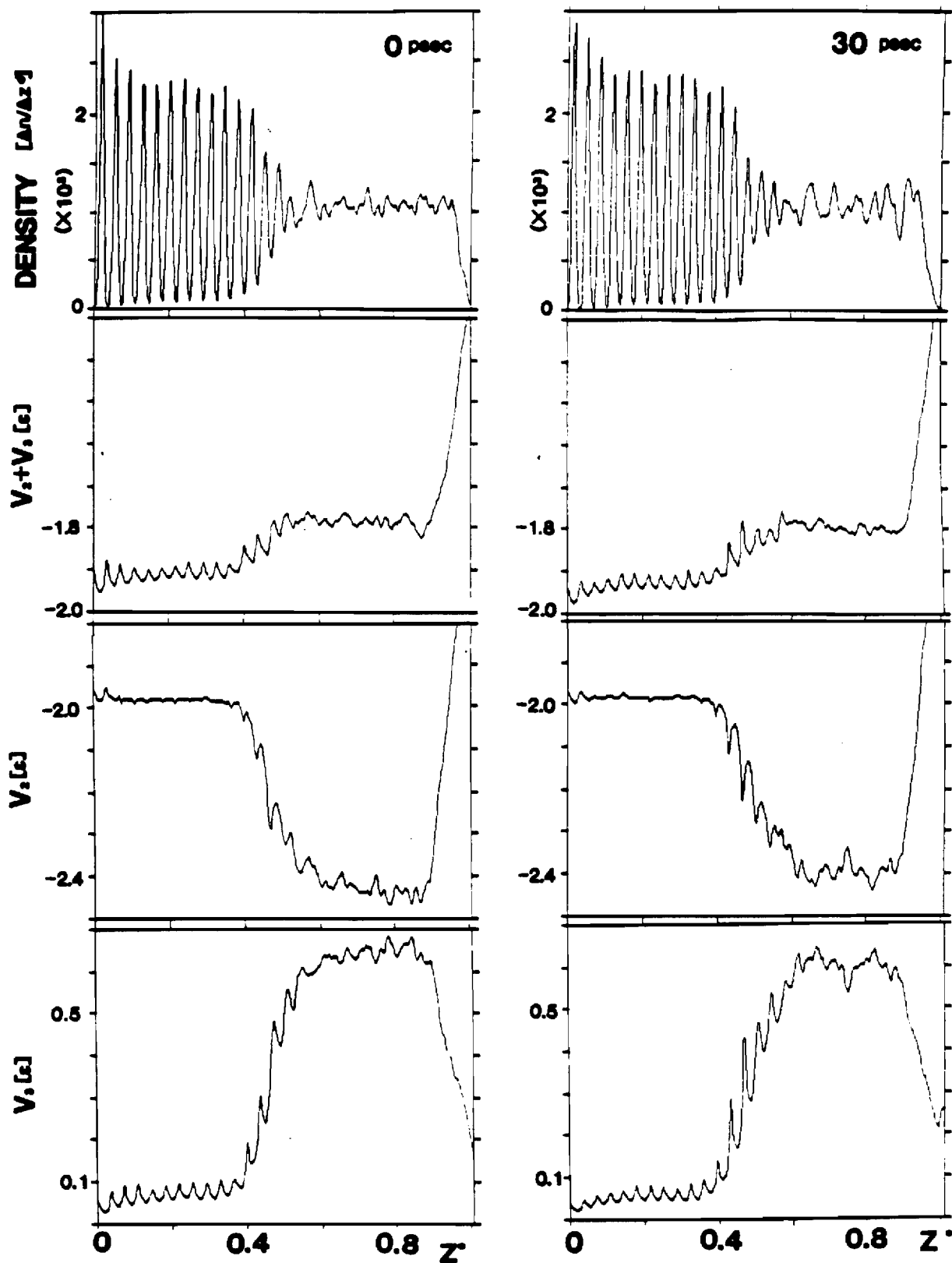


FIGURE 7

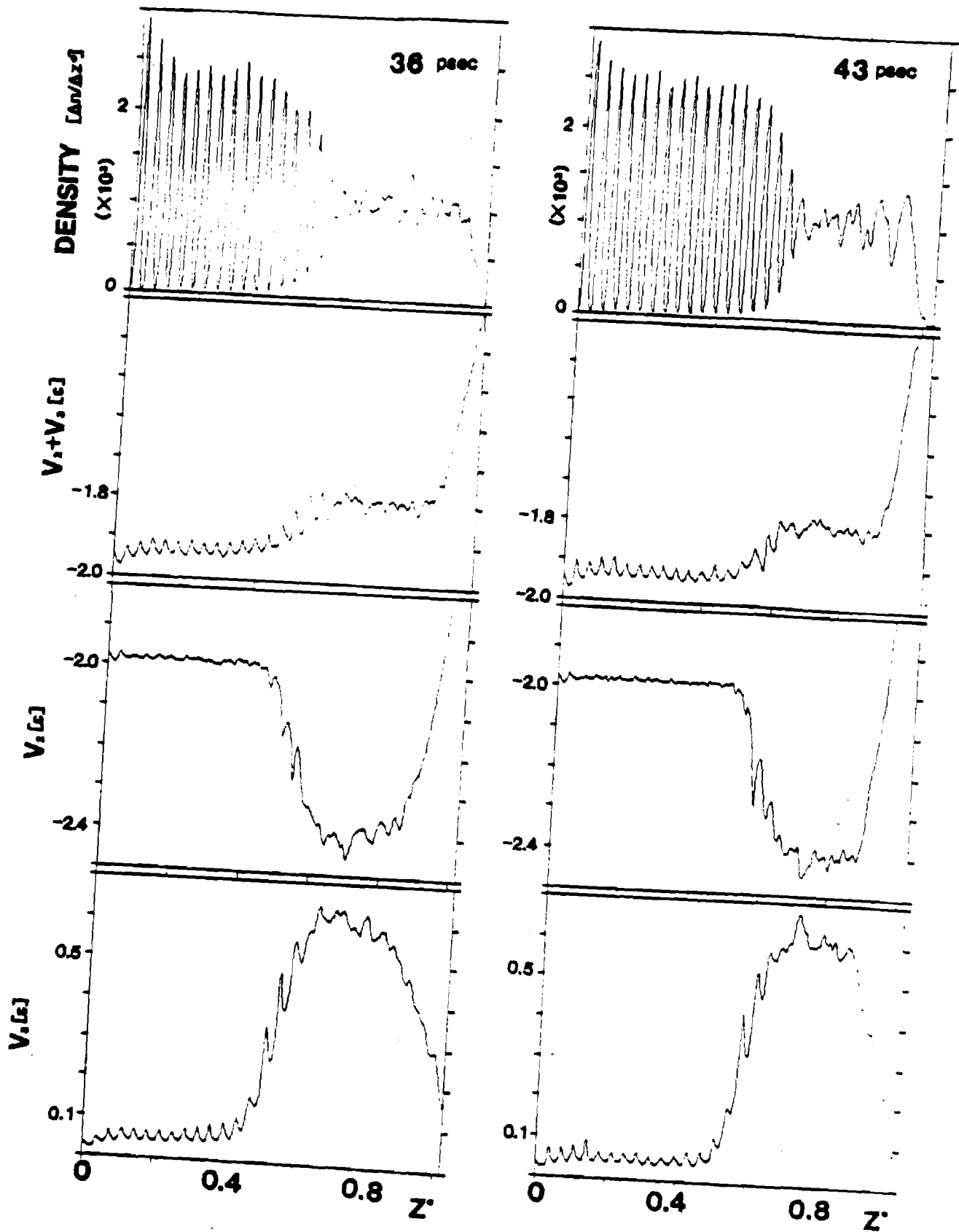


FIGURE 8

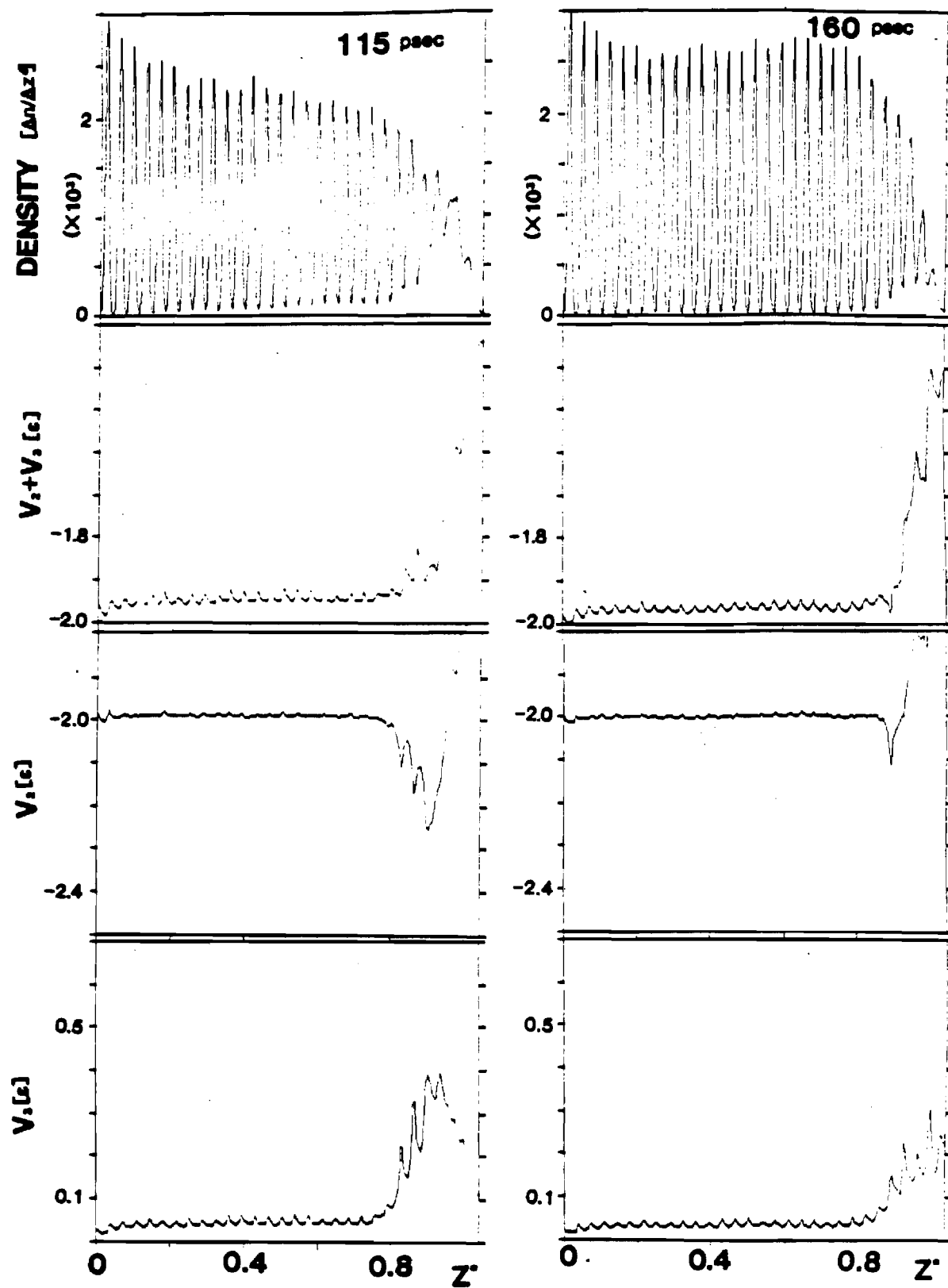


FIGURE 9

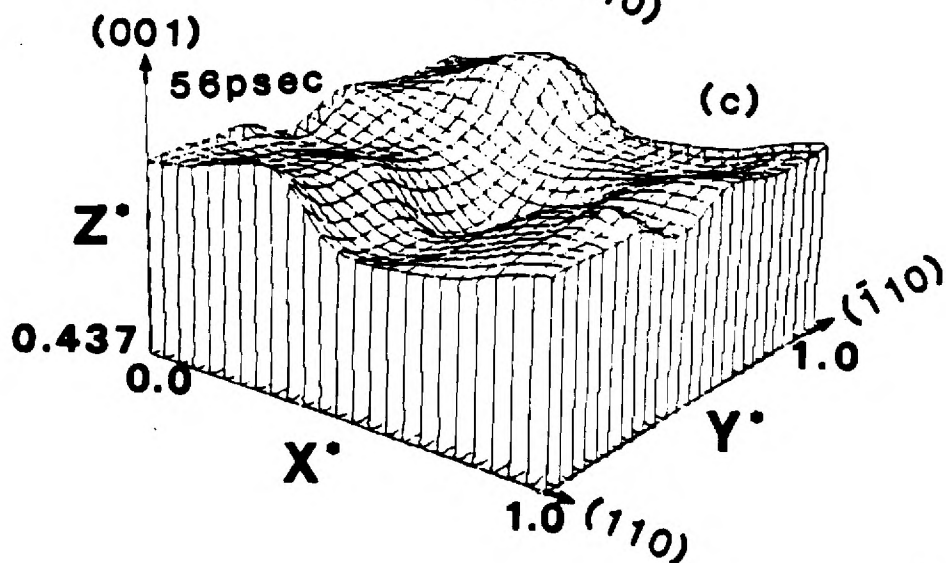
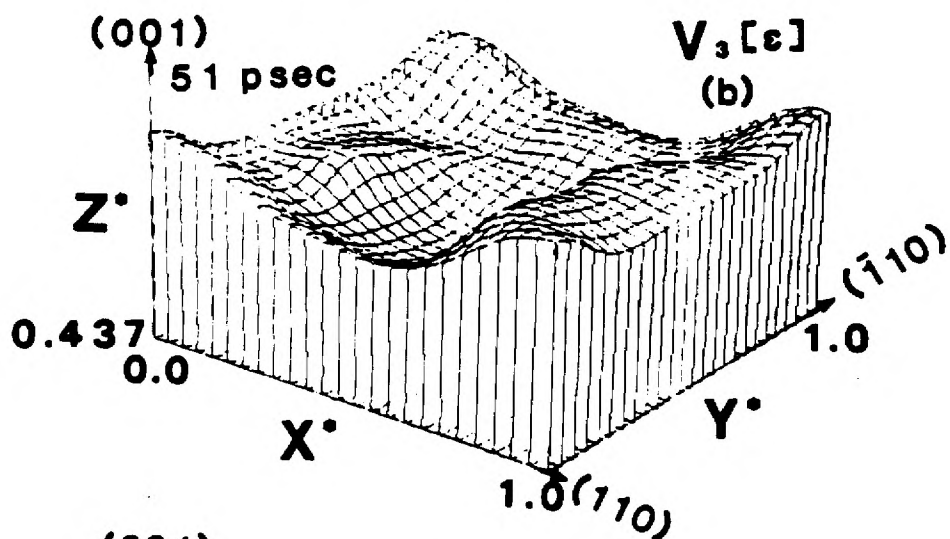
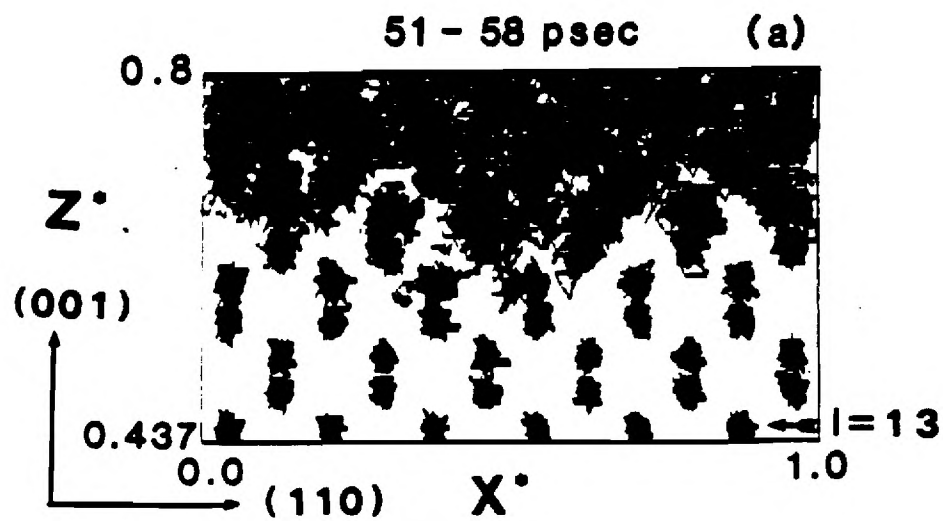


FIGURE 10

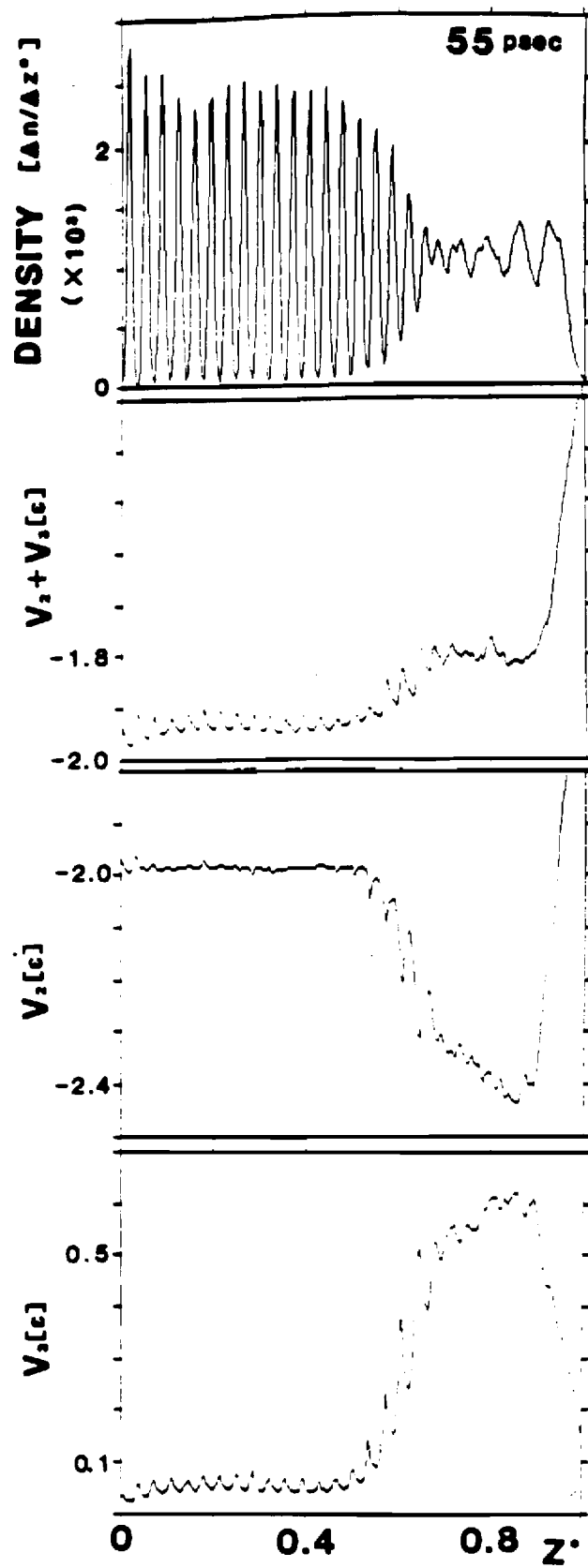


FIGURE 11

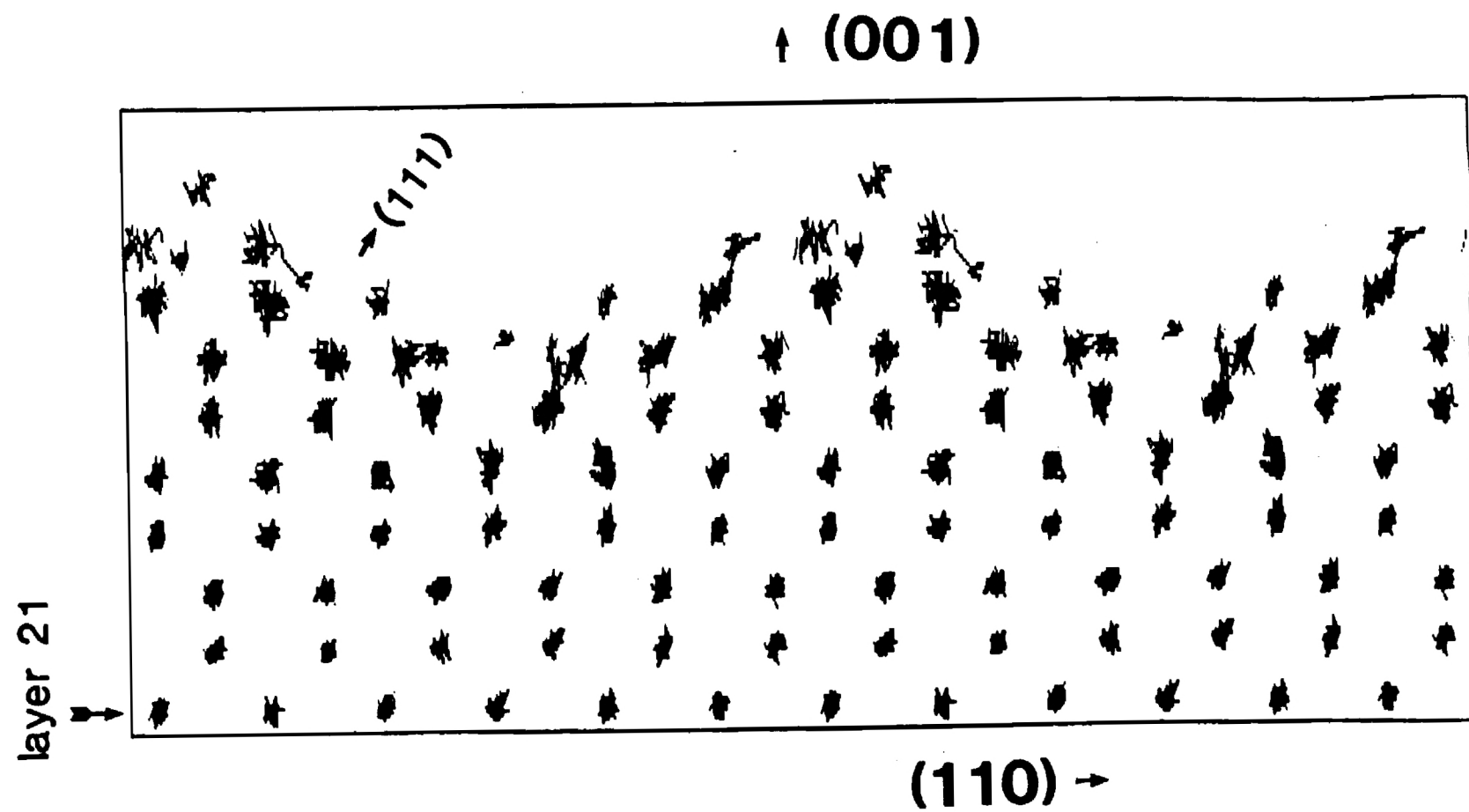


FIGURE 12

# Molecular Dynamics Simulations of Epitaxial Crystal Growth

## From the Melt: II. Si(111)

W. D. Luedtke, Uzi Landman, M. W. Ribarsky

R. N. Barnett and C. L. Cleveland

School of Physics, Georgia Institute of Technology,

Atlanta, Ga. 30332

### Abstract

Molecular Dynamics simulations are employed in studies of liquid-phase epitaxial growth onto a Si(111) surface. The material is described using two- and three-body interaction potentials which provide a realistic description of crystalline silicon and of the crystal-melt interface. Starting from a system at equilibrium solid-melt coexistence, it is driven out of equilibrium by allowing heat conduction to the underlying substrate. Two heat extraction rates are used resulting in growth velocities of 14 m/sec and 9 m/sec. The crystal grown under the faster growth conditions contains stacking faults, defective layers and an amorphous region. The slower growth results in a more perfect crystal with stacking faults and a narrow region of disorder at the solid-vacuum interface. Crystallization is initiated when the crystal-melt interface supercools by  $\sim 150\text{K}$  and a layer-by-layer growth mode is observed, accompanied by self-annealing processes. The dynamics of the crystal growth processes are investigated with refined spatial and temporal resolution using real space particle trajectories and following the evolution of the system temperature, potential energy and density profiles.



## I. Introduction

Crystal growth from the melt by liquid-phase epitaxy, is one of the oldest methods for growing crystals.<sup>1,2</sup> The development of fast pulsed laser material processing techniques, often called laser annealing, opens new avenues in crystal growth technology and provides new ways and means for detailed studies of phase transformations and growth of material systems.<sup>3-10</sup> In particular, the development of time resolved spectroscopic techniques and improved microscopy methods yield information on refined spatial and temporal scale which provide the impetus for the development of microscopic theoretical models of the physical processes which underlie phase-transformation and growth phenomena of materials. These developments, coupled with significant progress in the understanding of the nature of interactions and bonding in materials and in our computational capabilities, allow the formulation and implementation of computer simulations which are capable of providing realistic descriptions of material systems and of probing systematically the microscopic energetics and dynamics of processes in these systems.

In the first paper in this series<sup>11</sup> (see preceding paper, referred to as paper I), we have described in detail the development of computer molecular dynamics (MD) simulations and their application to studies of LPE on the (001) surface of silicon. In this paper we employ the methods developed in I for studies of the dynamics of LPE on the (111) surface of silicon. Orientational dependencies of the growth mode and characteristics of the growth processes in LPE (such as the growth rates, the types of defects and their generation mechanisms and the threshold interface velocity for amorphization) have been observed even at the high growth velocities occurring in pulsed laser

experiments.<sup>12-15,10</sup> In addition the orientational dependence of the growth velocity has been discussed in the context of Monte Carlo calculations based on a kinetic Ising model<sup>16</sup> of the crystal melt interface and MD simulations of face-centered cubic material employing Lennard-Jones (LJ) potentials.<sup>17-20</sup> Also, orientational dependencies of the diffuse structure and extent of the equilibrium solid-melt interface have been found using MD simulations employing LJ potentials<sup>17,19,21</sup> and more recently in simulations<sup>22,23</sup> employing two- and three-body interactions constructed<sup>24</sup> and parameterized to adequately describe the properties of tetrahedrally bonded materials, Si in particular. In these later studies it was found that the coexistence crystal-melt interfaces of Si(001) and Si(111) differ markedly. While the Si(111) crystal-melt equilibrium interface is characterized by a sharp, abrupt and flat transition from the crystal to the melt region, the interface for the (001) orientation is broad and structured, exhibiting a pronounced tendency for the formation of microfacets based on (111) planes.<sup>22</sup> In addition, the melt region in the vicinity of the solid-melt interface exhibits for both orientations a certain degree of ordering due to the underlying crystalline potential, resulting in a diffuseness of the interface at that region. As discussed in I<sup>11</sup> molecular dynamics simulations are ideally suited for studies of LPE since by following the time evolution of all particles of the system, the dynamics of the two phases (solid and liquid) which comprise the system is included. Thus cooperative dynamical effects (particularly of importance in the liquid) as well as the energetics of the system and interfacial kinetics are treated in these simulations on equal footing, unlike kinetic models where only the latter effects are considered.

Starting from an equilibrated system at solid-melt coexistence, with a (111) interface, we have investigated liquid-phase-epitaxial growth which was driven by allowing heat conduction to the substrate. In these investigations we have employed the same procedure of sample preparation and growth simulation as in our studies of LPE on the (001) surface (see paper I). Using the same cooling rate as the one used for the (001) surface, growth occurred at a velocity of 14 m/sec yielding a grown crystal which contained an assortment of defects (stacking faults, in-layer defects and a disordered region). Reducing the cooling rate by a factor of one half resulted in a growth velocity of 9 m/sec with the grown crystal possessing a markedly higher degree of perfection (stacking faults and a very narrow region of disorder limited to the crystal-vacuum interface). In the following we refer to these two simulations as the fast and slow studies, respectively. As in the case of the (001) system we find for both cooling rates of the (111) system that crystallization did not start until the temperature at the interface dropped, from the initial melting point temperature by about 150K. Once crystallization starts the crystal-melt interface propagates by a layer-by-layer growth mode with the interface maintaining a sharp character. We find however, that unlike growth on the (001) surface which occurred in an almost continuous, monotonous, manner, the advance of the crystallization front versus time in both (111) systems is discontinuous, with periods of crystallization interrupted by stages of no apparent forward movement of the interface. Close inspection reveals that during these stages self-annealing of defects occurs. As the defective region achieves a high level of structural perfection crystallization resumes.

Following a brief description of the set-up of the system we describe in the next section our results of LPE on the (111) surface of silicon, and discuss them in light of experimental observations.

## 2. Liquid Phase Epitaxy on Si(111)

The simulation system is constructed as a thick slab which is periodically repeated in two directions and is free, with no imposed boundary condition, in the third direction. Additionally it is positioned on top of a static substrate, composed of 4 layers, which is set up in [111] orientation with the Z axis parallel to the [111] crystallographic direction and the 2D cell is defined by the  $[\bar{1}10]$  and  $[10\bar{1}]$  directions. The number of layers,  $N_L$ , in the initial crystalline system (which was then partially melted via a heat pulse, as described in paper I) was 20 with 49 particles per layer (i.e., the total number of dynamic particles was 980). In the numerical integration of the equations of motion, using a fifth-order predictor-corrector algorithm, we employed a time step  $\Delta t = 1.15 \times 10^{-3}$  psec; with this choice and a frequent updating of the interaction lists (every 8  $\Delta t$ ), the total energy of the system is conserved to at least six significant figures (for a few thousand time-steps). All other technical details of the simulation and the interaction potentials are as described for the (001) system in paper I (see section 2). Throughout, energy and temperature are expressed in units of  $\epsilon = 50$  kcal/mole (to convert to temperature in Kelvins multiply the reduced temperature by  $2.517 \times 10^4$ ) and length in units of  $\sigma = 2.0951$  Å.

Starting from an equilibrated crystalline sample<sup>22</sup> at  $T = 0.064$  (1593K), a heat pulse was applied (via scaling of velocities) to the top 1/3 of the system and the system was allowed to evolve for  $1.5 \times 10^5$  time steps (~175

psec) yielding an equilibrated system at solid-melt coexistence at  $T_m = 0.0670 \pm 0.0020$  (1685°K). Particle trajectories (recorded for 2000  $\Delta t$ ) viewed along the  $[\bar{1}10]$  direction and in-layer trajectories for layers 10, 11 and 8,9 are shown<sup>22</sup> in Fig. 1(a), 1(b), and 1(c), respectively, along with the density (1d) and per-particle potential energy profiles (1e) in the (111) direction (with  $Z^* = \lambda \equiv 14.96\sigma$ , where  $\sigma = 2.0951 \text{ \AA}$ , and the unit of length in the  $[\bar{1}10]$  and  $[10\bar{1}]$  directions is  $12.85\sigma$ ). As evident from the figure the solid-melt interface is sharp, abrupt and flat (to be contrasted with the broad, structured, interface found for the equilibrium solid-melt interface of the (001) system,<sup>22</sup> see Fig. 2 of paper I). Additionally it is seen that though layer 10 is clearly identifiable in the particle density profile, particles in this region exhibit partial liquid-like characteristic as evident from the particle trajectories (Fig. 1(b)) and the high-value of the 3-body potential energy (Fig. 1(e)) at the location corresponding to the occurrence of the layer in the density profile.

Having obtained an equilibrium system the growth simulations were initiated by extracting heat from the system via scaling of particle velocities in the bottom two layers, as described in paper I. Two simulation experiments were performed. One in which the rate of heat extraction was as that used for the (001) system (i.e., scaling of velocities every 5  $\Delta t$  such as to remove at a constant rate an amount of energy which is equal to the latent heat per layer every 6 psec) and the other where half the above rate was used (the "fast" and "slow" simulations, respectively).

The time evolutions of the overall system temperature and of the 3-body and 2-body contributions to the potential energy of the system are shown in Figs. 2 and 3 for the "fast" and "slow" simulations, respectively. In both

cases, in the initial stage of the simulation the system temperature drops continuously, as a result of the heat conduction to the substrate, with no significant ordering observed. Once the temperature has dropped to a certain level (see below) crystallization is initiated, as noted in the figures ( $\sim 43$  psec and 58 psec for the fast and slow systems, respectively). The time developments of both systems exhibit a characteristic non-monotonous behavior (particularly pronounced in the potential energies (Figs. 2(b,c) and 3(b,c))). This behavior should be contrasted with the monotonous, continuous changes found for the (001) system (see paper I, Fig. 3), and is due to differences in the growth modes for these two crystalline orientations. As we discussed above the Si(111) solid-melt interface is structurally different and less complex than that for the Si(001) system, exhibiting a flat morphology. In addition, in the present system, the influence of the crystalline potential on the melt adjacent to it extends over a rather narrow region, resulting in a more abrupt interface. These characteristics pertain not only to the equilibrium state but maintain during growth. As a result growth on the (111) surface occurs in a layer-by-layer manner. The above mentioned discontinuities in the growth rate are related to the ordering processes in each of the added layers. An additional effect characteristic to the (111) system is seen at  $\sim 70$  psec for the fast system (Fig. 2) and  $\sim 140$  psec for the slow one (Fig. 3), where a marked change in the rate of crystallization occurs, accompanied by a period of almost constant temperature. As we discuss below this effect is associated with self-annealing processes and subsequent fast growth.

In Figs. 4 and 5 profiles of the system temperature (in units of  $\epsilon = 50$  kcal/mole) versus  $Z^*$  ( $Z^* = 1 = 14.96\sigma$ ) at selected times are shown, for the fast and slow simulation, respectively. These profiles were obtained as

short-time averages ( $2 \times 10^3 \Delta t$ ) and therefore they exhibit a degree of noise. In both systems we observe that during the initial cooling period preceding crystallization, the temperature drops throughout the system below the initial ( $t = 0$ ) melting point temperature. Crystallization starts ( $t = 43$  psec in Fig. 4 and 58 psec in Fig. 5) when the temperature at the solid-melt interface drops to  $\lesssim 0.06$ , which corresponds to an undercooling of  $\geq 150^\circ\text{K}$ .

In the following we present first the results for LPE under high-velocity growth conditions followed by those for the slower velocity growth.

#### High-Velocity Growth

In order to investigate the details of the growth process we present in Figs. (6-9) profiles of the particle densities,  $\Delta n / \Delta Z^*$  vs  $Z^*$  along the [111] direction, and profiles of the per-particle potential energy,  $V_2 + V_3$ , and those for the individual contributions,  $V_2$  and  $V_3$ , recorded at selected times during the simulation. Since the system is in a non-equilibrium state, dynamically evolving in time, these profiles were obtained as short-time averages ( $\sim 10^3 \Delta t$ ) and therefore they contain a degree of noise. We were forced however to employ such short averaging times in order to capture the temporal characteristics of the system at selected times during the growth process. Thus, while in the solid region the pronounced maxima in the density profiles and the corresponding minima in the potential energies occur at the locations of crystalline layers, occasionally the random displacement of a small number of particles into the spacing between crystalline layers shows up in the potential energy profiles as spikes (whereas inspection of the density profile at those locations indicates good crystalline order). No such occurrences are seen in the liquid region since, even for the short averaging times which we used, the diffusion of particles in the melt averages out such spurious features.

Inspection of the profiles shown in Fig. 6 at  $t = 0$  and 30 psec reveals that during this time period no crystallization occurred. From Fig. 4 and Fig. 2 we observe that during this time period the temperature of the system drops to a little over 0.06. As seen from Fig. 4 (compare the temperature profiles at 30 psec and 43 psec) and Fig. 2 the temperature continued to decrease to below 0.06 (a supercooling of over  $150^{\circ}\text{K}$ ). Concomitant with this degree of supercooling (similar to that found in the Si(001) system at the final stages of the cooling period) we observe by comparing the profiles at  $t = 43$  psec shown in Fig. 7 to those at  $t = 30$  psec that growth started to occur, and the interface advanced by that time by adding at least one crystalline layer to the solid, (note the drops in the values of  $V_3$  at the locations of layers 11 and 12 in the corresponding density profile). During the subsequent 15 psec an additional layer (number 13) starts to grow and a refinement of the structure of the neighboring underlying crystalline region occurs, as the  $t = 58$  psec profiles in Fig. 7 demonstrate. At this time the advance of the crystallization front slows significantly as evident from the profiles shown in Fig. 8 at  $t = 72$  psec and  $t = 87$  psec. In contrast, in the time period between 87 psec and 101 psec (see Fig. 9) growth resumes with the addition of 2-3 layers at the latter time.

A closer look at the evolution of the system between  $t = 58$  psec and  $t = 101$  psec is provided by the real-space particle trajectories, viewed along the  $[\bar{1}10]$  direction, and inlayer trajectories for layers 10-13, shown in Fig. 10. Comparison of the position of the interface, in the top of the figure, for  $t = 58, 72$  and 87 psec indicates that it did not advance during this time period. The inlayer particle trajectories at  $t = 58$  psec reveal a defective region in crystalline layer 10 (see lower left portion), which induces a similar



defective region in layer 11 above it. These defects persist at a later time ( $t = 72$  psec), until at  $t = 87$  psec they are annealed (note the constancy of  $V_3$  during at this time period, in Fig. 2). Once the inlayer defect was annealed vigorous growth resumed as evident from the trajectories shown for  $t = 101$  psec (see also Fig. 2). This sequence of events demonstrates an interesting phenomena of dynamical self-annealing in which the evolving system self-corrects structural errors, thus improving the quality of the grown crystal. We also found evidence for this mechanism in the simulation of the slow growth velocity system.

Views of the system towards the end of the simulation are given by the profiles in Fig. 9 ( $t = 158$  psec) and the real-space particle trajectories, viewed along the  $[1\bar{1}0]$  direction in Fig. 11. From the original location of the solid-melt interface and the final location of the top of the grown crystal and the time which lapsed between these two states we estimate the growth velocity as  $\sim 14$  m/sec.

The structure of the grown crystal (see Fig. 11) reveals a crystalline region with perfect intralayer order but containing "mistakes" in the registry of layers (stacking faults), as well as a region of defective layers and a wide region of a disordered solid, closer to the solid vacuum interface. We also note that towards the end of the simulation the temperature of the system dropped significantly, such that activation barriers for defect annealing and disorder-order transformations cannot be surmounted. As will be shown below the structural quality of the grown crystal is dramatically improved upon reducing the growth velocity.

#### Low-Velocity Growth

We turn now to presentation of the results for the slow-rate growth system. As indicated in Fig. 3 in the first stage after the start of the heat

conduction to the substrate, the system undercools with no significant growth occurring. The temperature profiles shown in Fig. 5 demonstrate that by 58 psec the temperature at the interface region dropped to  $\lesssim 0.06$ , and as an inspection of the density and potential energy profiles shown in Fig. 12 indicates by about that time growth has begun. We note from the temperature profile in Fig. 5 ( $t = 58$  psec) that crystallization in this system occurs while the temperature in the melt region ( $Z^* > 0.6$ ) is higher than in the crystalline part. Comparison of the profiles at 58 (Fig. 12) psec and those recorded about  $t = 72$  psec demonstrates the slow growth (Fig. 13). We also observe that during the next 72 psec only about one additional layer grew. At about  $t = 144$  psec radical changes in the rates of variation of the overall system temperature and potential energies are evident (see Fig. 3). The constancy of the temperature starting at about that time and sharp drops in  $V_3$  and  $V_2$  signify growth at a much faster rate than before that time as is evidenced by comparing the density and potential energy profiles for  $t = 158$  psec in Fig. 14 with those at  $t = 144$  psec (Fig. 13). From the temperature profile of the system at  $t = 158$  psec (see Fig. 5), during the growth period, we observe that the faster progress of the crystallization front occurs when the interface region is at a temperature of  $\sim 0.058$  while the crystalline material is at a lower temperature thus forming a gradient.

The final stages of the simulation are described by the profiles at  $t = 259$  (Fig. 14) and the real-space particle trajectories, viewed along the  $[110]$  direction, shown in Fig. 15. From the last figure we conclude that at the present growth velocity, estimated as  $\sim 9$  m/sec, a crystal possessing a high degree of structural perfection was grown. We observe in it stacking faults and a very narrow band of defective layers and disorder limited to the immediate vicinity of the solid-vacuum interface.

### 3. Discussion

In this paper (and in paper I<sup>11</sup>) we have developed a methodology for molecular dynamics studies of equilibrium and non-equilibrium interfaces and have employed it in investigations of liquid phase epitaxial growth of silicon on the (111) and (001) surfaces, using interaction potentials which include 2 and 3-body contributions and provide an adequate description of the material. As discussed and demonstrated in paper I, growth on the (001) surface at high-interface velocity ( $\sim 18$  m/sec) involved an undercooled, structured, microfaceted solid-melt interface and proceeds in a continuous, monotonous manner yielding a structurally perfect grown crystal. Comparison of our results for the two surfaces highlights the orientational dependence of the growth processes, which was experimentally observed,<sup>10,12-15</sup> and provides insights into the nature of liquid-phase epitaxy. As discussed in paper I (see section 4) it is pertinent to discuss the results of our studies in light of the information obtained in laser-annealing experiments.

In the first stage of our simulations a system at equilibrium, solid-melt coexistence at the melting point, was prepared. The melting point of the system was determined to be  $0.067 \pm 0.0020$  (1685<sup>0</sup>K) in good agreement with the experimental melting point of Si (1683<sup>0</sup>K). The latent heat which we estimated from the difference of the average potential energies in the solid and melt region is 31.4 kJ/mole, compared to the experimental value of 50.7 kJ/mole. The solid-melt interface in equilibrium is characterized as sharp, abrupt and flat, in contrast to the microfaceted, broad, structured interface found for the equilibrium interface of the (001) system.<sup>11</sup>

Starting from the equilibrium state, the system was cooled by extracting energy from the bottom two-layers of the dynamical system, which are sufficiently removed from the interface region such that the effect of heat extraction (via scaling of velocities every 5  $\Delta t$ ) does not interfere with the dynamical evolution of the system in that region. As described in the previous section, two rates of cooling were employed. In the "fast" rate simulations, which resulted in a growth velocity of  $\sim 14$  m/sec, the constant rate of heat extraction was 61.25 kcal/mole $\cdot$ psec, and in the "slow" simulations, resulting in a growth velocity of 9 m/sec, the cooling rate was 30.625 kcal/mole $\cdot$ psec. These rates of energy removal correspond to cooling rates of  $\sim 2 \times 10^{12}$   $^{\circ}$ K/sec and  $\sim 1 \times 10^{12}$   $^{\circ}$ K/sec, respectively. We note that these cooling rates are in the range of values which may be achieved in laser-annealing experiments.<sup>15</sup> As in the case of the (001) system,<sup>11</sup> in the initial stage after heat conduction to the substrate started, the temperature of the system drops with no discernable crystallization observed. In both the "fast" and "slow" cooling simulations, ordering and crystallization began only when the overall system temperature dropped below the melting point and the supercoolings in the interface regions were  $\geq 200^{\circ}$ K and  $\sim 150^{\circ}$ K, respectively (see Figs. 4 and 5). These degrees of supercooling are similar to that which we found for the (001) system (for the "fast" system, which was cooled at the same rate as the (001) system, the observed supercooling is somewhat higher). The crystallization which ensued past the initial cooling stage, for both cooling rates, is characterized as discontinuous (nonmonotonous) with periods of rapid crystallization interrupted by stages of cessation of the propagation of the interface. This behavior, which contrasts with the monotonous growth rate in the (001) system indicates a difference in the growth modes for these

two crystalline orientations. The flat, abrupt, solid-melt interface in the (111) system ~~maintains~~ during growth. Since in this system the spatial variation of the crystalline potential extends over a rather narrow region, it affects only the melt particles in its immediate vicinity and growth occurs via a layer-by-layer mechanism. Furthermore we have found that growth is accompanied by dynamical self-annealing processes which provide a mechanism for structural perfection. We observed that occasionally propagation of the crystallization front is halted and then is resumed after a certain period of time ( $\sim 30\text{--}50$  psec). Closer inspection reveals that these events are related to the occurrence of defects in a newly crystallized layer which then induce the generation of defects in the subsequent crystallizing layers above it. The proliferation of these defects stops further motion of the interface. During the halting period annealing processes take place. Once the structural perfection has been restored, vigorous crystallization resumes. These self-annealing processes are characteristic to the (111) system and are connected with the ease with which defects can occur in this system as compared with that for the (001) orientation (related to the smoothness of the interface and the fact that Si(111) requires the formation of triple and single bonds). We also find that such self-annealing processes become more predominant at high growth velocities. In this context we note that for the same cooling rate, growth on the (001) system proceeded at a higher rate ( $\sim 18$  m/sec) than on the (111) system ( $\sim 14$  m/sec, obtained in the "fast" simulations) in agreement with observations<sup>12-14</sup> and previous theoretical studies.<sup>16</sup> Moreover, unlike the case for the (001) system, the crystal grown on the (111) surface at high-velocity is imperfect, containing stacking faults, defective layers and a wide region of disordered material. We note

that the mistakes in registry (stacking faults) involve perfectly ordered layers and occur closer to the start of the crystallization stage than the generation of defective layers and disordered region, which start to occur only later, after the temperature of the system drops significantly and activation barriers for defect self-annealing cannot be surmounted. The perfection of the grown crystal is markedly improved by reducing the cooling rate, resulting in a lower growth velocity ( $\sim 9$  m/sec) and yielding a grown crystal containing stacking faults and only a narrow region of disorder, limited to the immediate vicinity of the solid-vacuum interface. These observations correlate well with experimental observations<sup>12-15</sup> (see in particular reference 13) and provide a microscopic understanding of the nature and mechanisms of epitaxial growth.

#### Acknowledgement

This work was supported by U. S. Department of Energy under grant No. FG05-86ER45234 and in part by a grant from the North-American Philips Corporation. The computations were performed on the CRAY-XMP at the National Magnetic Fusion Energy Computer Center, Livermore, California.

### References

1. Current Topics in Material Science, Vol. 2, 1976, Crystal Growth and Materials, Eds., E. Kaldis and H. J. Scheel (North-Holland, Amsterdam, 1977).
2. Crystal Growth: A Tutorial Approach, Eds. W. Bardsley, D. T. J. Hurle and J. B. Mullin (North-Holland, Amsterdam, 1979).
3. Laser-Solid Interactions and Laser Processing - 1978, AIP Conference Proc. No. 50, Eds., S. D. Ferris, H. J. Leamy and J. M. Poate, (AIP, New York, 1979).
4. Laser and Electron-Beam Interactions with Solids, Eds., B. R. Appleton and G. K. Celler, (North-Holland, Amsterdam, 1982).
5. Laser-Solid Interactions and Transient Thermal Processing of Materials, Eds., J. Narayan, W. L. Brown and R. A. Lemons, (North-Holland, Amsterdam, 1983).
6. Energy Pulse Modifications of Semiconductors and Related Materials (Vols. 1 and 2), Eds., K. Hennig, (Akad. der Wissenschaften der DDR, Rossendorf, 1984).
7. Laser Annealing of Semiconductors, Eds., J. M. Poate and J. W. Mayer (Academic Press, New York, 1982).
8. Semiconductors and Semimetals, Vol. 23: Pulsed Laser Processing of Semiconductors, Eds., R. F. Wood, C. W. White and R. T. Young, (Academic Press, Orlando, 1984).
9. See review by K. A. Jackson in: Surface Modification and Alloying, Eds., J. M. Poate, G. Foti and D. C. Jacobson (Plenum, New York, 1983) Ch. 3.
10. See review by J. M. Poate, J. Cryst. Growth 79, 549 (1986).

11. U. Landman, W. D. Luedtke, M. W. Ribarsky, R. N. Barnett and C. L. Cleveland, preceeding paper.
12. See review by: A. G. Cullis, in Ref. 7, Chapt. 6, p. 147; C. W. White, B. R. Appleton, and S. R. Wilson, *ibid.* Chapt. 5, p. 111; C. W. White, in Ref. 8, Chapt. 2, p. 43; J. M. Poate, *Mat. Res. Soc. Sym. Proc.* 4, 121 (1982).
13. A. G. Cullis, N. G. Chew, H. C. Weber and D. J. Smith, *J. Cryst. Growth* 68, 624 (1984).
14. A. G. Cullis, H. C. Weber, N. G. Chew, J. M. Poate, and P. Baeri, *Phys. Rev. Lett.* 49, 219 (1982).
15. R. Tsu, R. T. Hodgson, T. Y. Yan and J. E. E. Baglin, *Phys. Rev. Lett.* 42, 1358 (1979).
16. G. H. Gilmer in Ref. 5, p. 249.
17. U. Landman, C. L. Cleveland and C. S. Brown, *Phys. Rev. Lett.* 45, 2032 (1980); U. Landman, C. L. Cleveland, C. S. Brown, and R. N. Barnett, in Nonlinear Phenomena of Phase Transitions and Instabilities, Ed. T. Riste (Plenum, N. Y., 1982), p. 379.
18. C. L. Cleveland, U. Landman and R. N. Barnett, *Phys. Rev. Lett.* 49, 790 (1982).
19. U. Landman, R. N. Barnett, C. L. Cleveland and R. H. Rast, *J. Vac. Sci. Technol.* A3, 1574 (1985).
20. J. Q. Broughton, G. H. Gilmer and K. A. Jackson, *Phys. Rev. Lett.* 49, 1996 (1982).
21. See references in a review by F. F. Abraham, *J. Vac. Sci. Technol.* B2, 534 (1984); See articles in Fluid Interfacial Phenomena, Ed., C. A. Croxton, (Wiley, Chichester, 1986); U. Landman, R. N. Barnett, C. L. Cleveland, W. D. Luedtke, M. W. Ribarsky, D. Scharf and J. Jortner, *Mat. Res. Soc. Symp. Proc.* 63, 273 (1985).



22. U. Landman, W. D. Luedtke, R. N. Barnett, C. L. Cleveland, M. W. Ribarsky, E. Arnold, S. Ramesh, H. Baumgart, A. Martinez and B. Khan, Phys. Rev. Lett. 56, 155 (1986).
23. F. F. Abraham and J. Q. Broughton, Phys. Rev. Lett. 56, 734 (1986).
24. F. H. Stillinger and T. A. Weber, Phys. Rev. B31, 5262 (1985).

### Figures

Figure 1: (a) Particle trajectories recorded at equilibrium, viewed along the  $[\bar{1}\bar{1}0]$  direction.<sup>22</sup> (b)-(c) In-plane trajectories, exhibiting solid and melt characteristics, in layers 10, 11 and 8, 9, viewed along the  $[111]$ ,  $Z^*$  direction.  $Z^* = 1 \equiv 14.96\sigma$  and the unit of length in the  $[\bar{1}\bar{1}0]$  and the  $[10\bar{1}]$  directions is  $12.85\sigma$ .  
 (d) Equilibrium particle density,  $\Delta n/\Delta Z^*$ , vs  $Z^*$ .  
 (e) Per-particle total and three-body potential energies,  $V_2 + V_3$  and  $V_3$  vs  $Z^*$ .

Figure 2: Time development of the system temperature,  $T$ , in units of  $\epsilon$  ( $\epsilon = 50$  kcal/mole) and of the per particle 3-body and 2-body contribution to the potential energy throughout the growth simulation of the "fast" heat extraction system, starting from the beginning of the heat extraction at  $t = 0$ . The start of the crystallization stage is noted ( $\sim 43$  psec). Note the nonmonotonous character of the process.

Figure 3: Same as Figure 2, for the "slow" heat extraction system. The start of the crystallization stage is noted ( $\sim 58$  psec). Note the nonmonotonous character of the process.

Figure 4: Temperature,  $T$ , profiles at selected times during the simulation of the "fast" Si(111) system. The  $t = 0$  profile was recorded for the equilibrium solid-melt coexistence system. All profiles were obtained as short-time averages over  $2 \times 10^3 \Delta t$ .

Figure 5: Same as Figure 4, for the "slow" Si(111) system.

Figure 6: Profiles of the particle density  $\Delta n / \Delta Z^*$ , where  $\Delta n$  is the number of particles with  $Z^*$  coordinates between  $Z^*$  and  $Z^* + \Delta Z^*$ , and profiles of the per particle total potential energy,  $V_2 + V_3$ , and of the 2-body and 3-body contributions ( $V_2$  and  $V_3$ , respectively) versus  $Z^*$  ( $Z^* = 1 \equiv 14.96\sigma$ ), at  $t = 0$  and 30 psec for the "fast" Si(111) system. In the crystalline region maxima in the density profiles and the corresponding minima in the potential energy profiles occur at the crystalline layer positions. Comparison of the profiles for the two times demonstrates that no significant crystallization occurred during the initial cooling stage.

Figure 7: Same as Figure 6 for  $t = 43$  psec (start of the crystallization stage, see Fig. 2) and  $t = 58$  psec. Comparison of the profiles at the two times demonstrates growth.

Figure 8: Same as Fig. 6 for  $t = 72$  and 87 psec. Comparison of the profiles at  $t = 58$  psec (Fig. 7) and those in this figure demonstrates the interruption in the advance of the crystallization during the time period  $t = 58 - 87$  psec (see also the temperature and potential energy profiles in Fig. 2 during this time period).

Figure 9: Same as Fig. 6 for  $t = 101$  psec and close to the end of the simulation at 158 psec. Comparison of the  $t = 101$  psec profiles to those in Fig. 8 demonstrates the resumption of the solid-melt interface propagation.

Figure 10: Top - real-space particle trajectories, viewed along the  $[\bar{1}\bar{1}0]$  direction, recorded at the denoted times (58 psec - 101 psec) during the simulation of the "fast" Si(111) system. Comparison of the real space trajectories at these times demonstrates the inter-

ruption in the crystallization front advance during  $t = 58 - 87$  psec and the resumption of progress at 101 psec. Bottom - inlayer particle trajectories at the corresponding times (recorded for  $10^3 \Delta t$ ). Note the defect (located at the lower left) in layer 10 at  $t = 58$  psec and 72 psec which induces the occurrence of a defective region above it, in layer 11, at these times. By time  $t = 87$  psec, the defective region in layer 10 was annealed as was the one layer 11, inducing a higher degree of order in layers 12 and 13. By time  $t = 101$  psec all four layers exhibit perfect inlayer crystalline order. This sequence demonstrates a self-annealing process.

Figure 11: Real space particle trajectories of the fast Si(111) system, viewed along the  $[\bar{1}\bar{1}0]$  direction, at the end of the simulation. The grown crystal contains stacking faults, defective crystalline layers and an amorphous region. The distance from bottom to top of the incised boundaries is  $14.96\sigma = 31.34 \text{ \AA}$ .

Figure 12: Particle density and potential energy profiles for the "slow" Si(111) system at equilibrium  $t = 0$ , and at  $t = 58$  psec, shortly after the beginning of the crystallization process.

Figure 13: Same as Fig. 12 for  $t = 72$  and 144 psec. Comparison of the profiles at 72 psec and those at 58 psec (Fig. 12) show interruption of the advancement of the crystallization front. Comparison between the profiles at 72 psec and 144 psec demonstrates the slow growth which occurred during this time period. At  $t = 144$  psec a fast growth stage occurs (see following figure and Fig. 3).

Figure 14: Same as Fig. 12 for  $t = 158$  and 259 psec, demonstrating fast growth during this period (see the sharp drop in  $V_3$ , and  $V_2$ , and the constant temperature period in Fig. 3, starting at  $t = 145$  psec).

Figure 15: Real space particle trajectories of the slow Si(111) system, viewed along the  $[\bar{1}\bar{1}0]$  direction, at the end of the simulation. The grown crystal shows a high degree of structural perfection. It contains stacking faults and a narrow region of inlayer defects and disorder, limited to the immediate solid-vacuum interface.

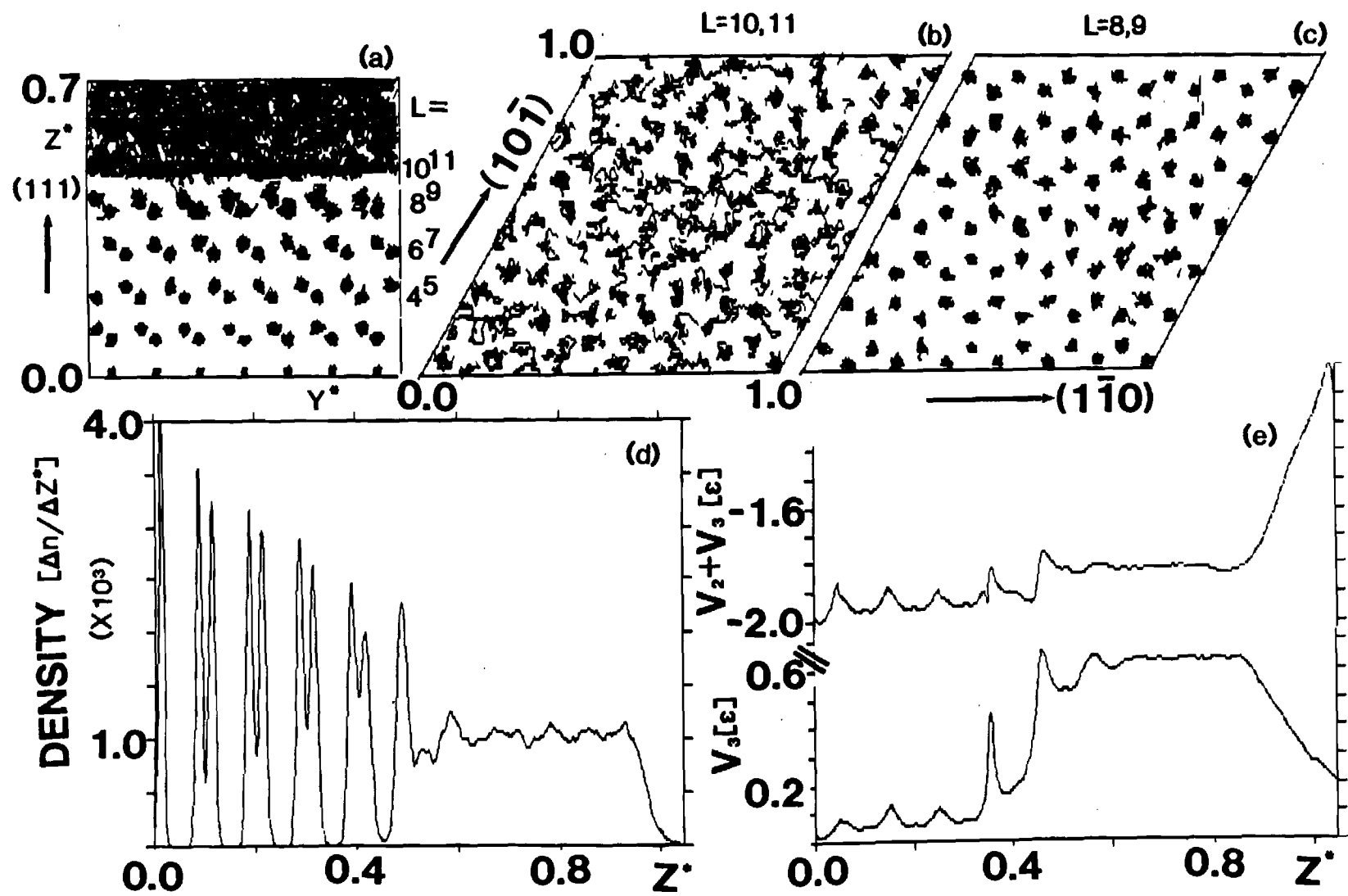


FIGURE 1

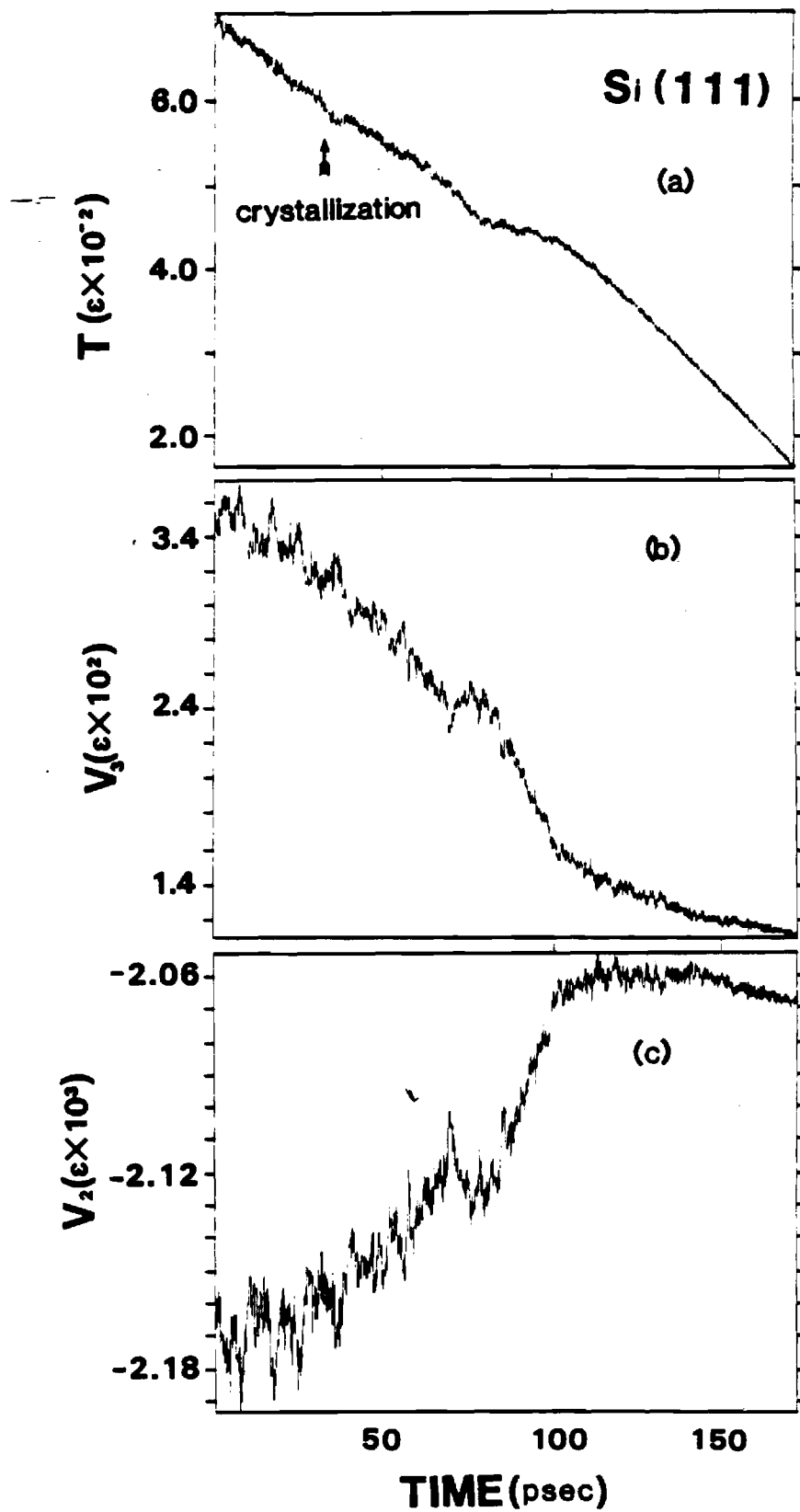


FIGURE 2

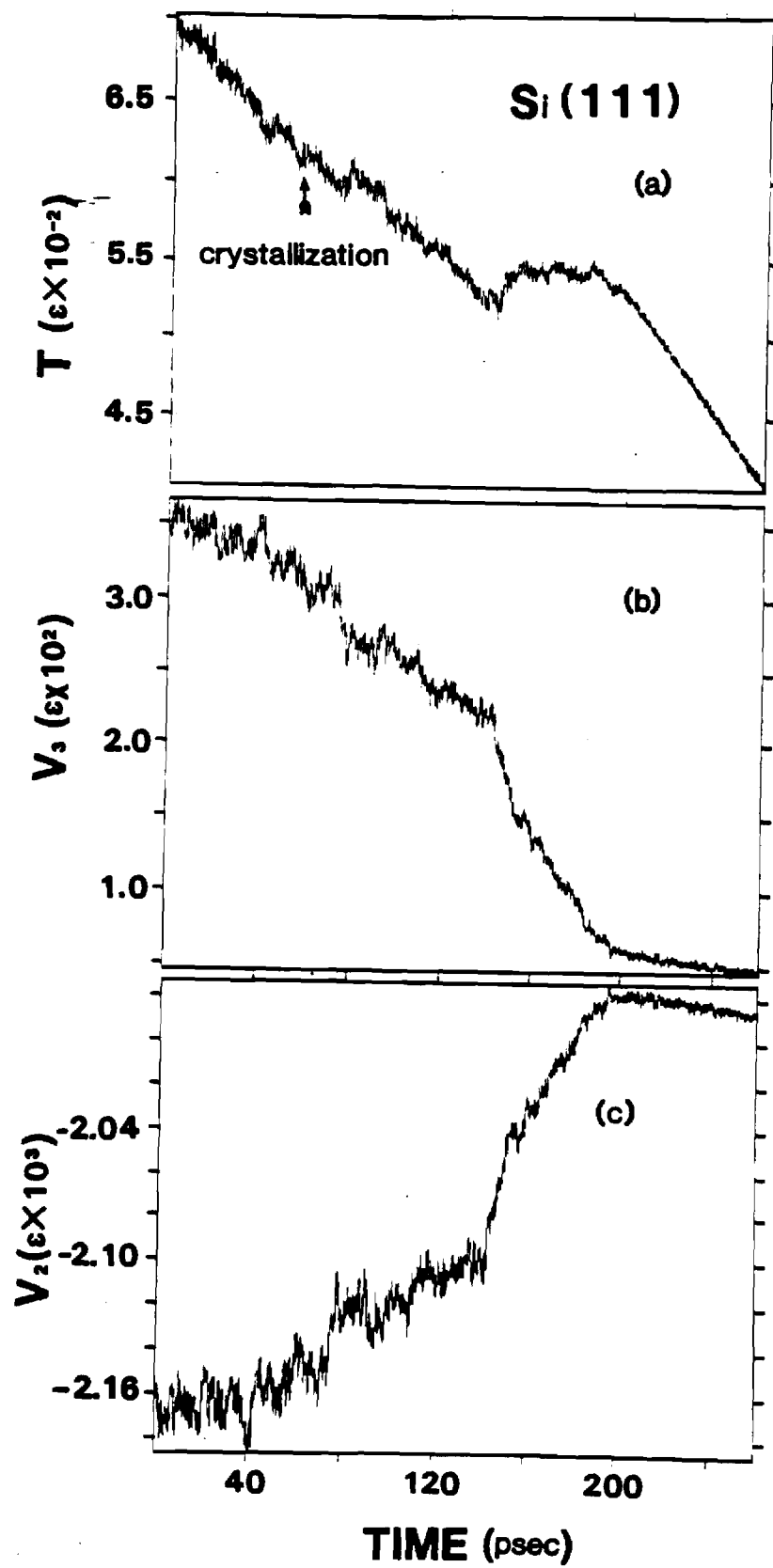


FIGURE 3



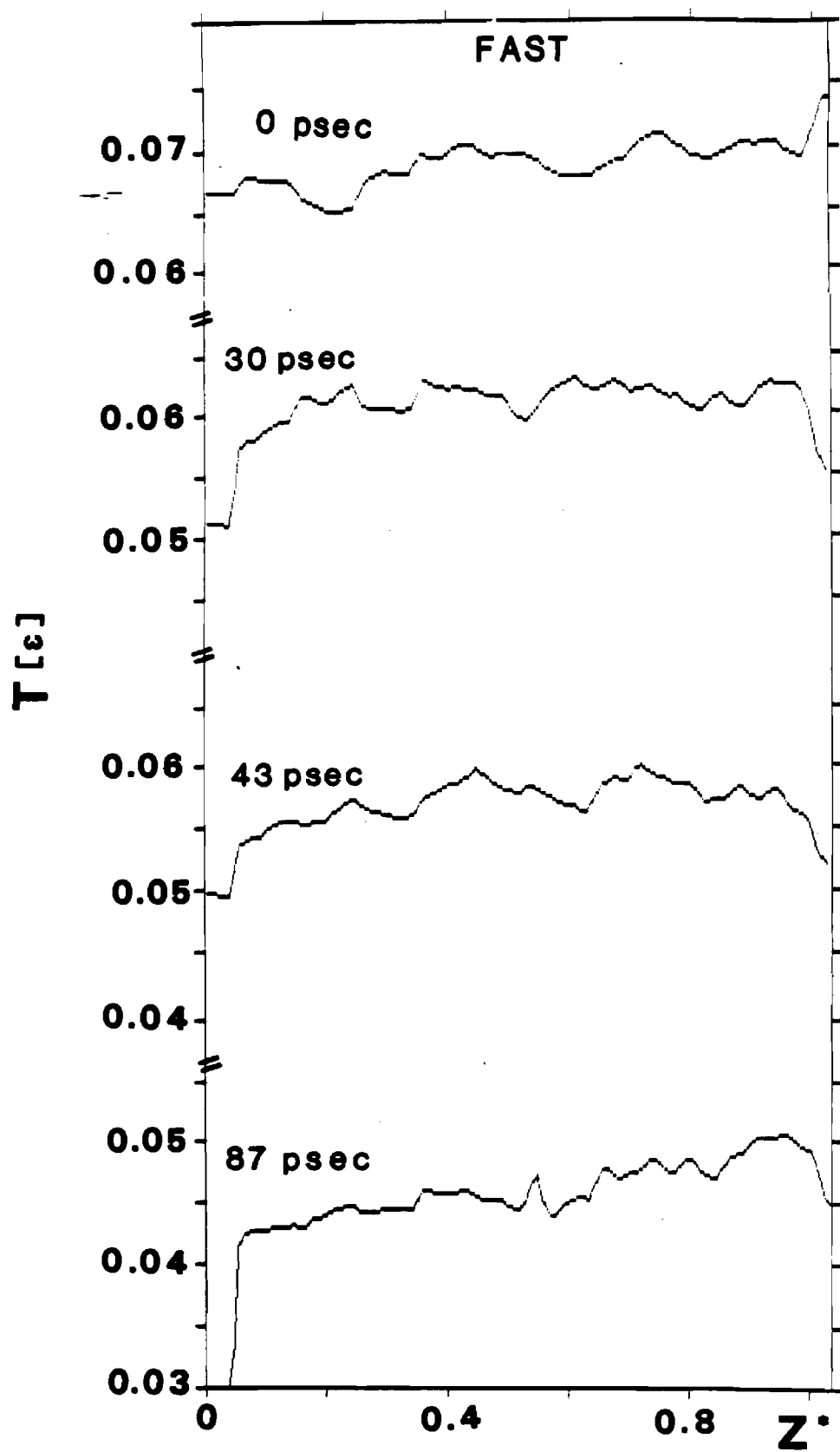


FIGURE 4

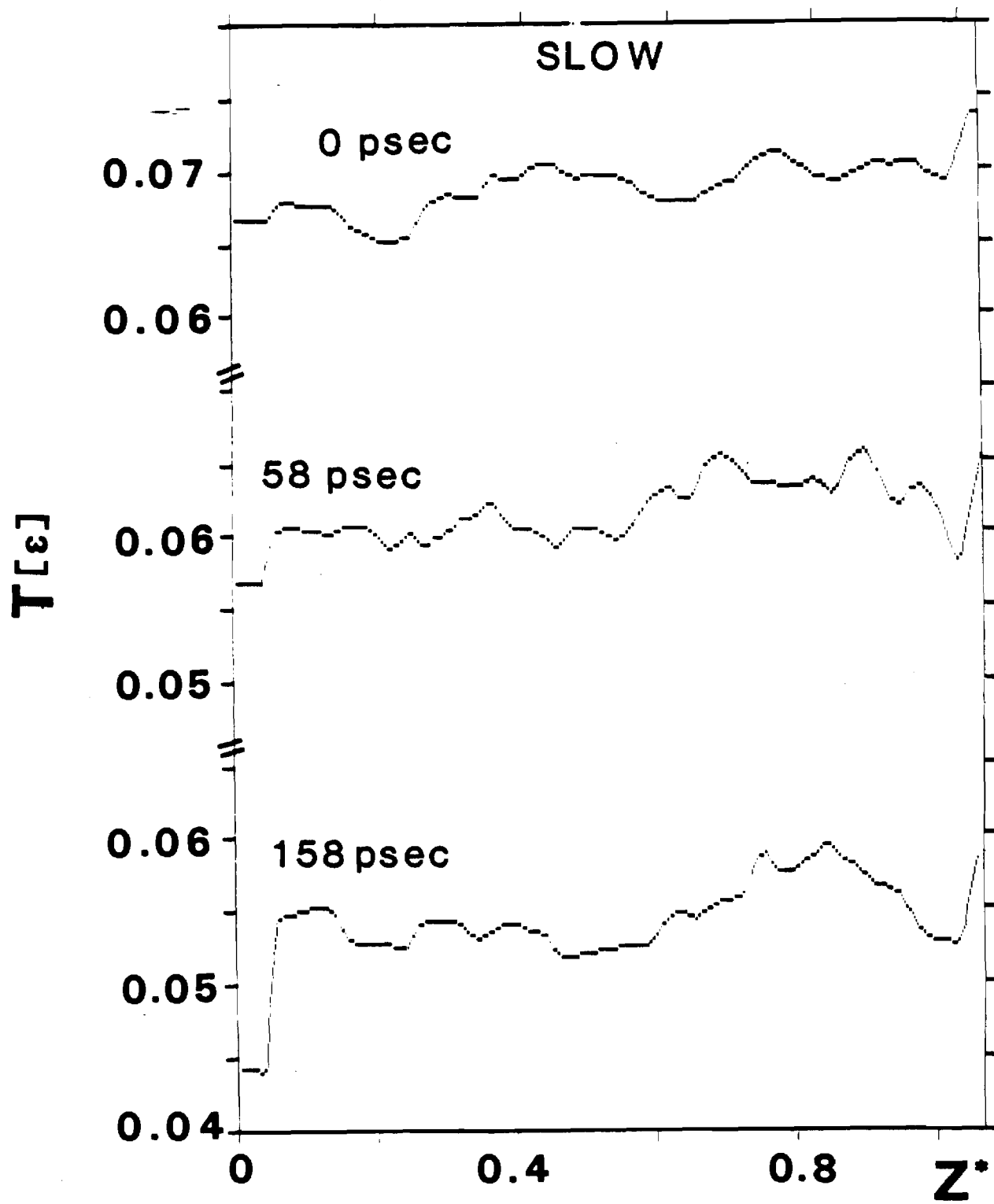


FIGURE 5

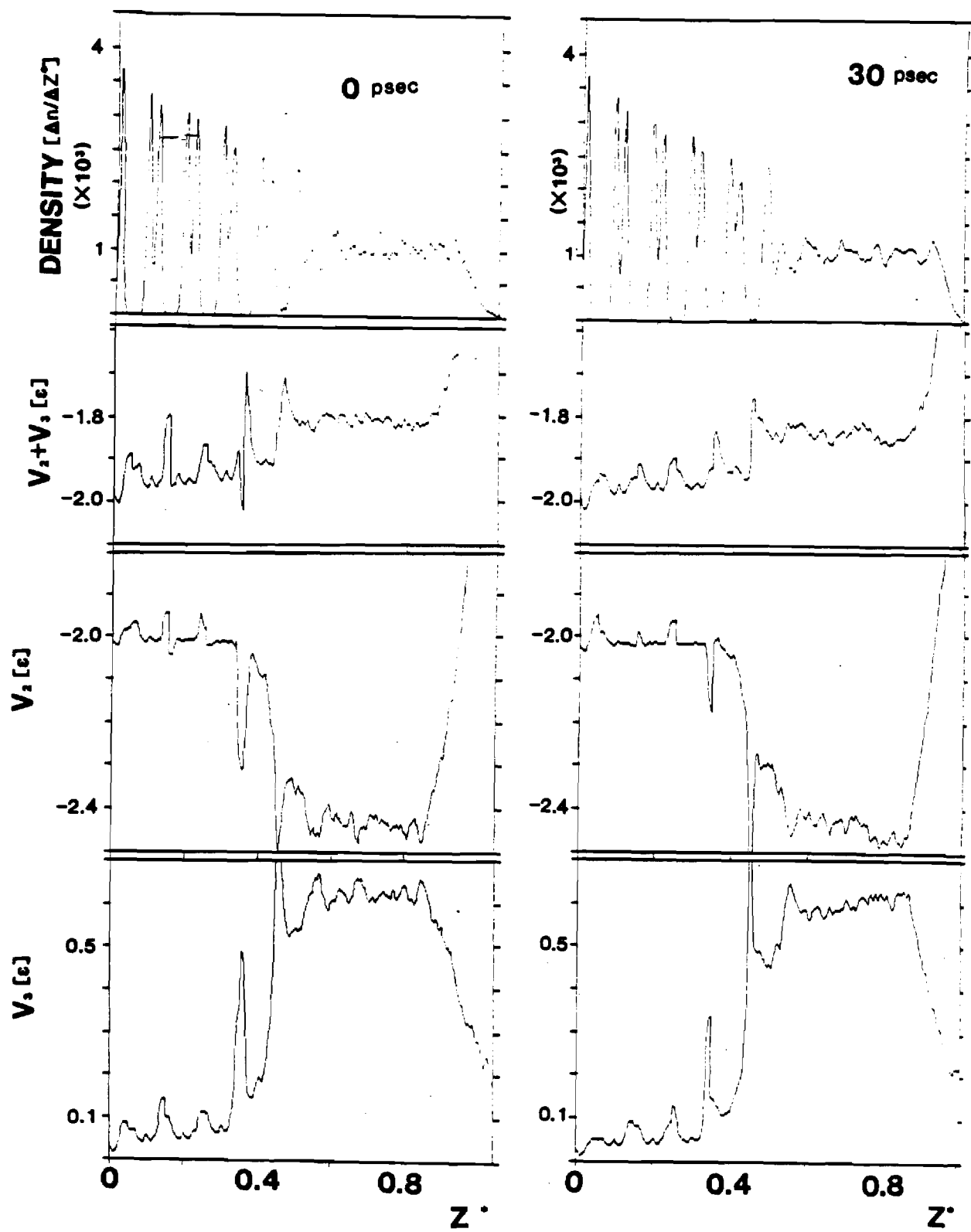


FIGURE 6

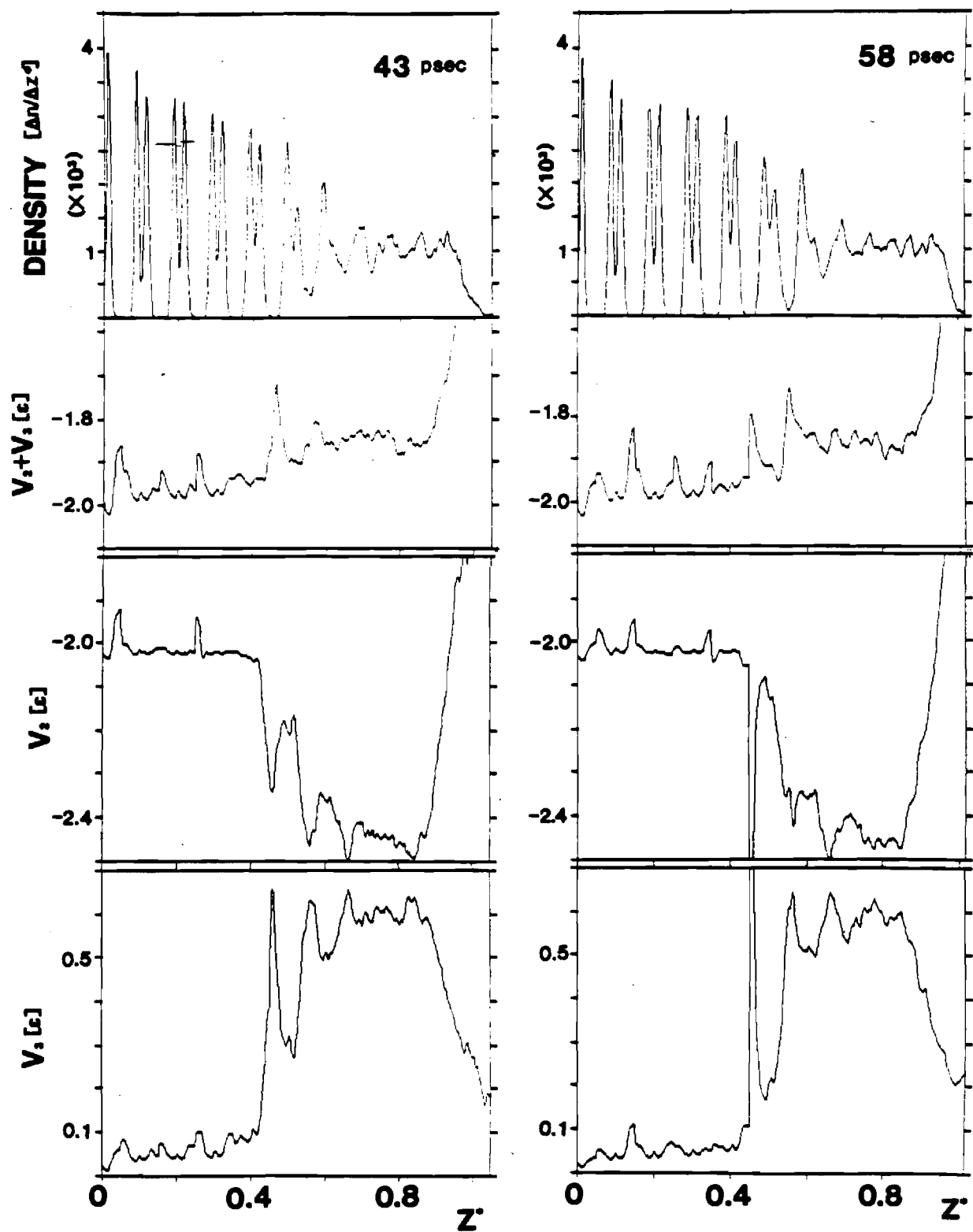


FIGURE 7

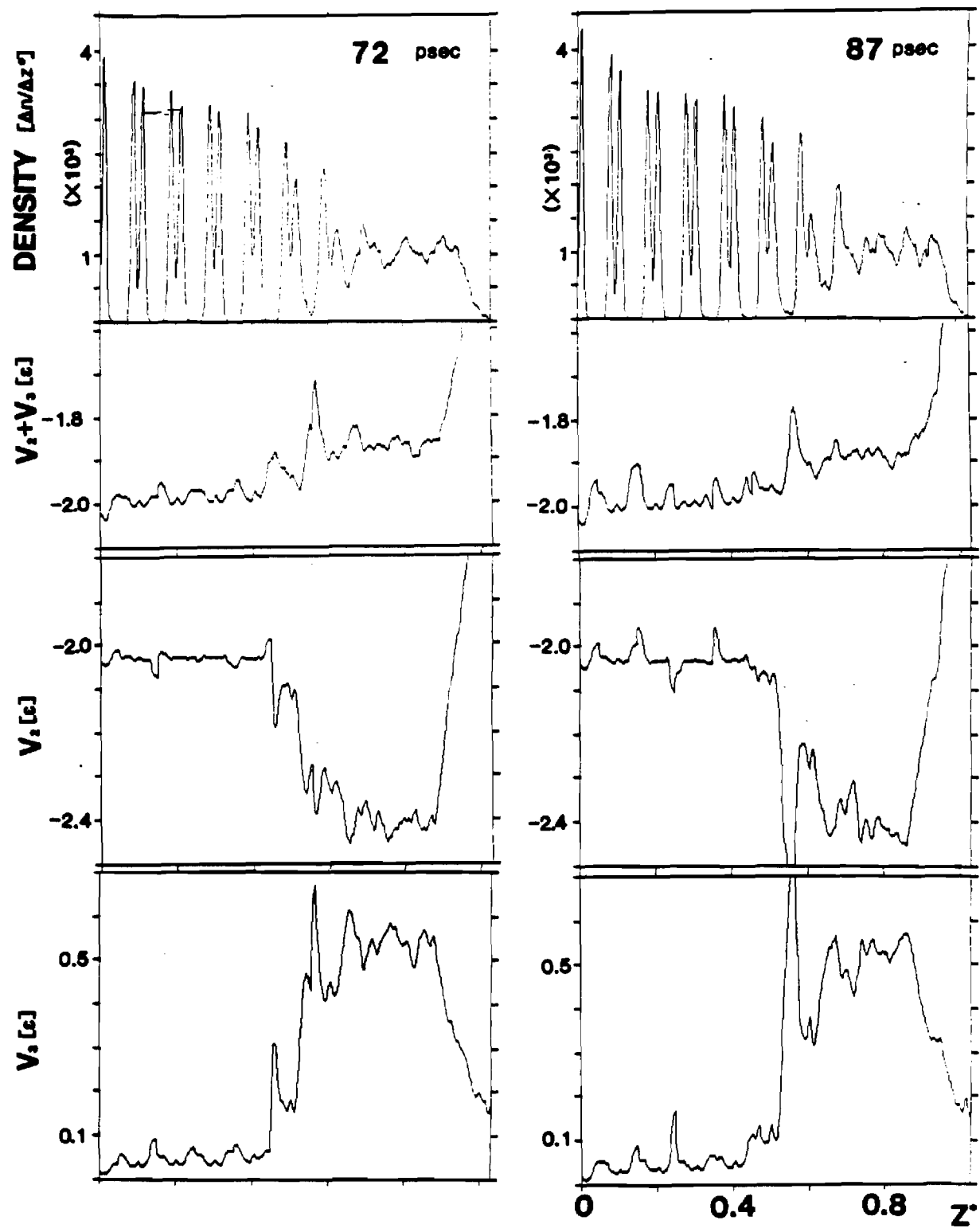


FIGURE 8

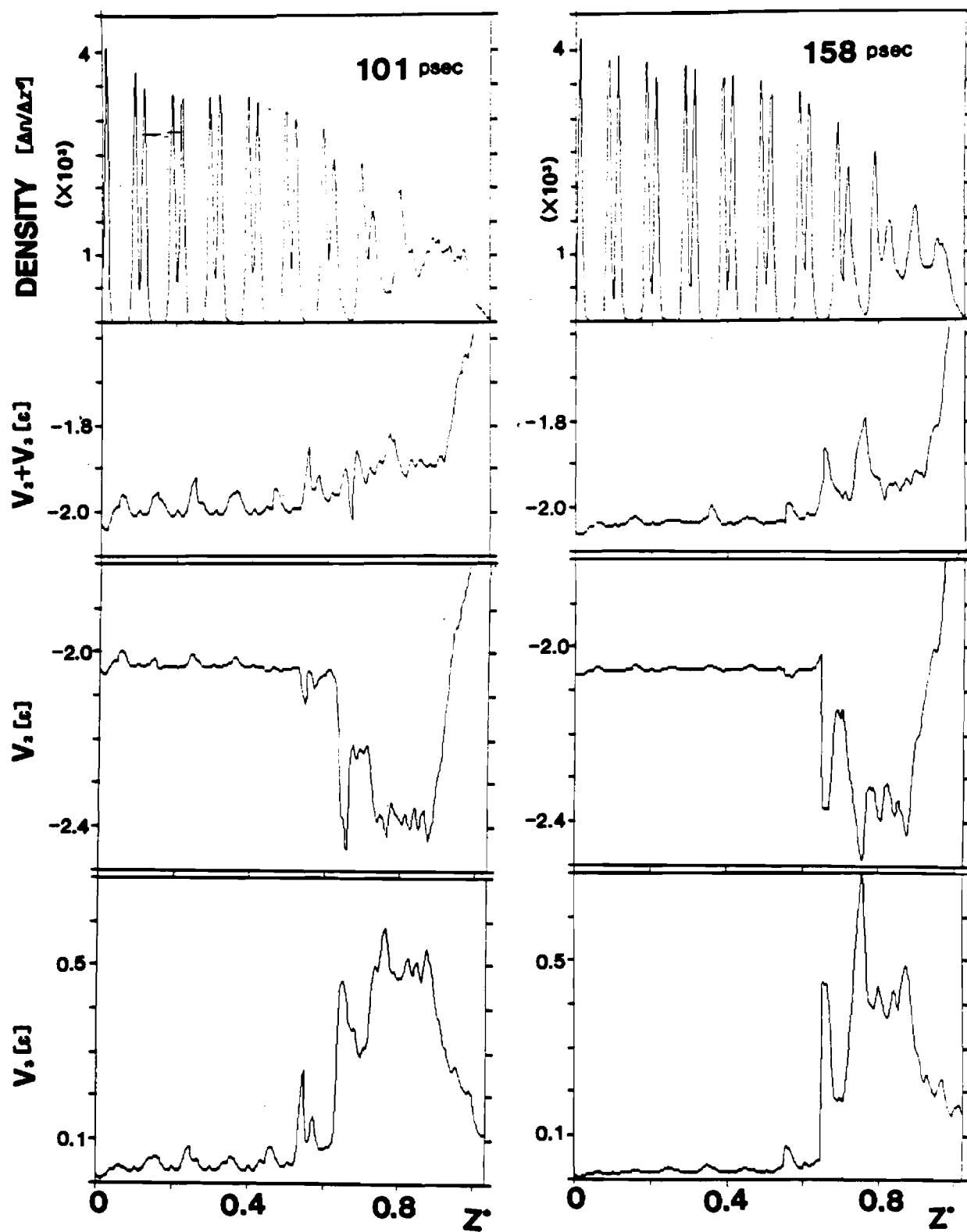


FIGURE 9

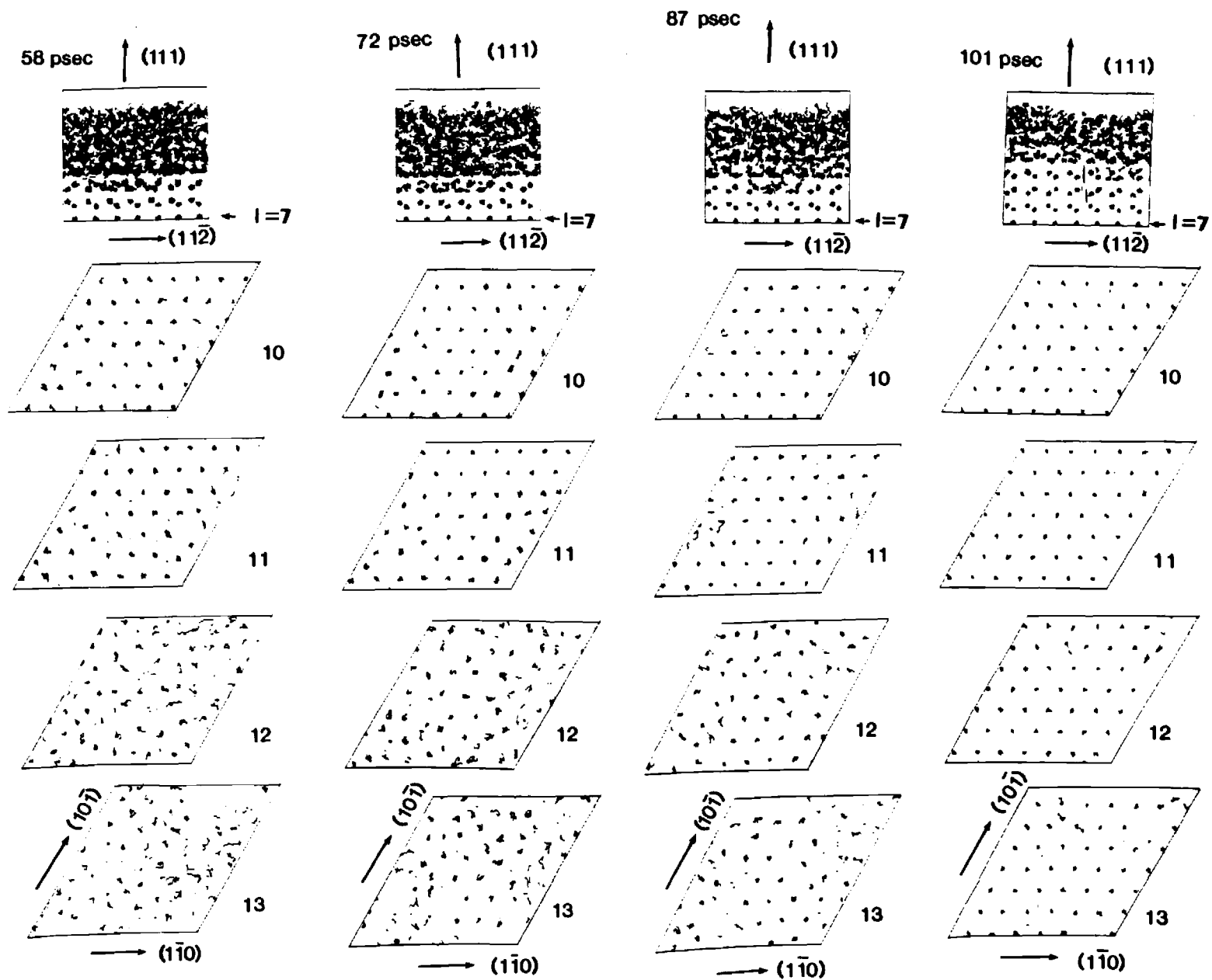


FIGURE 10

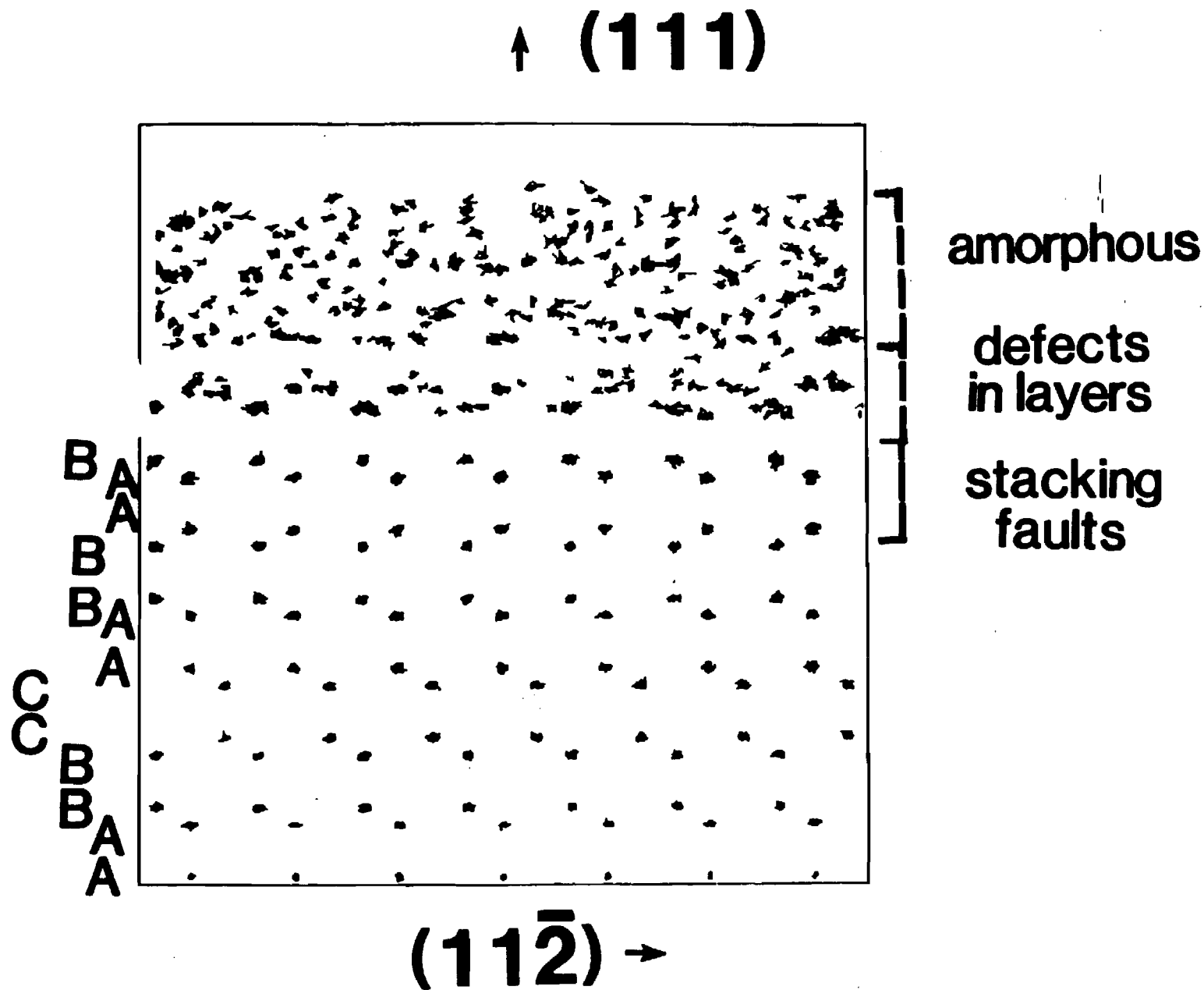


FIGURE 11



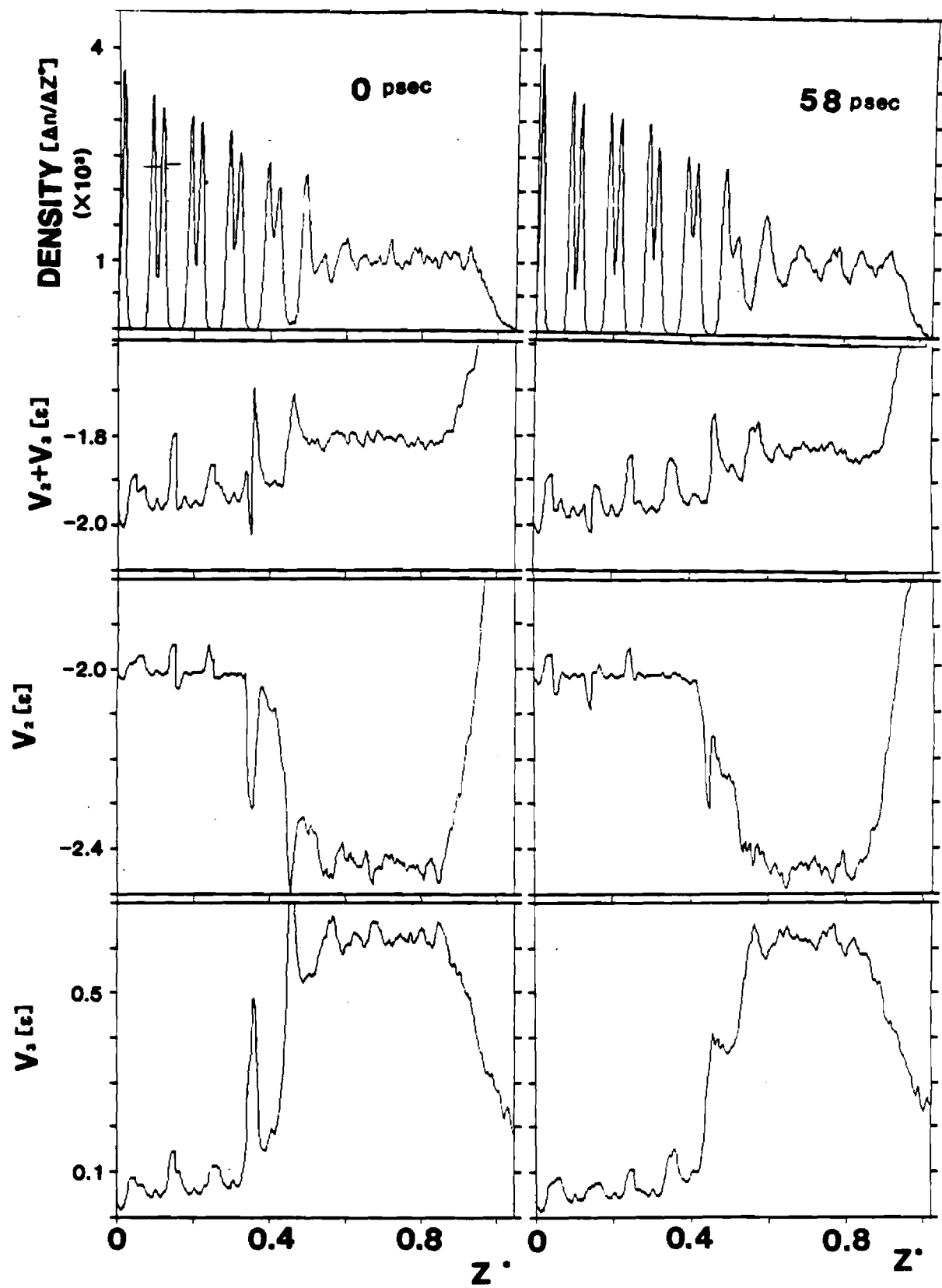


FIGURE 12

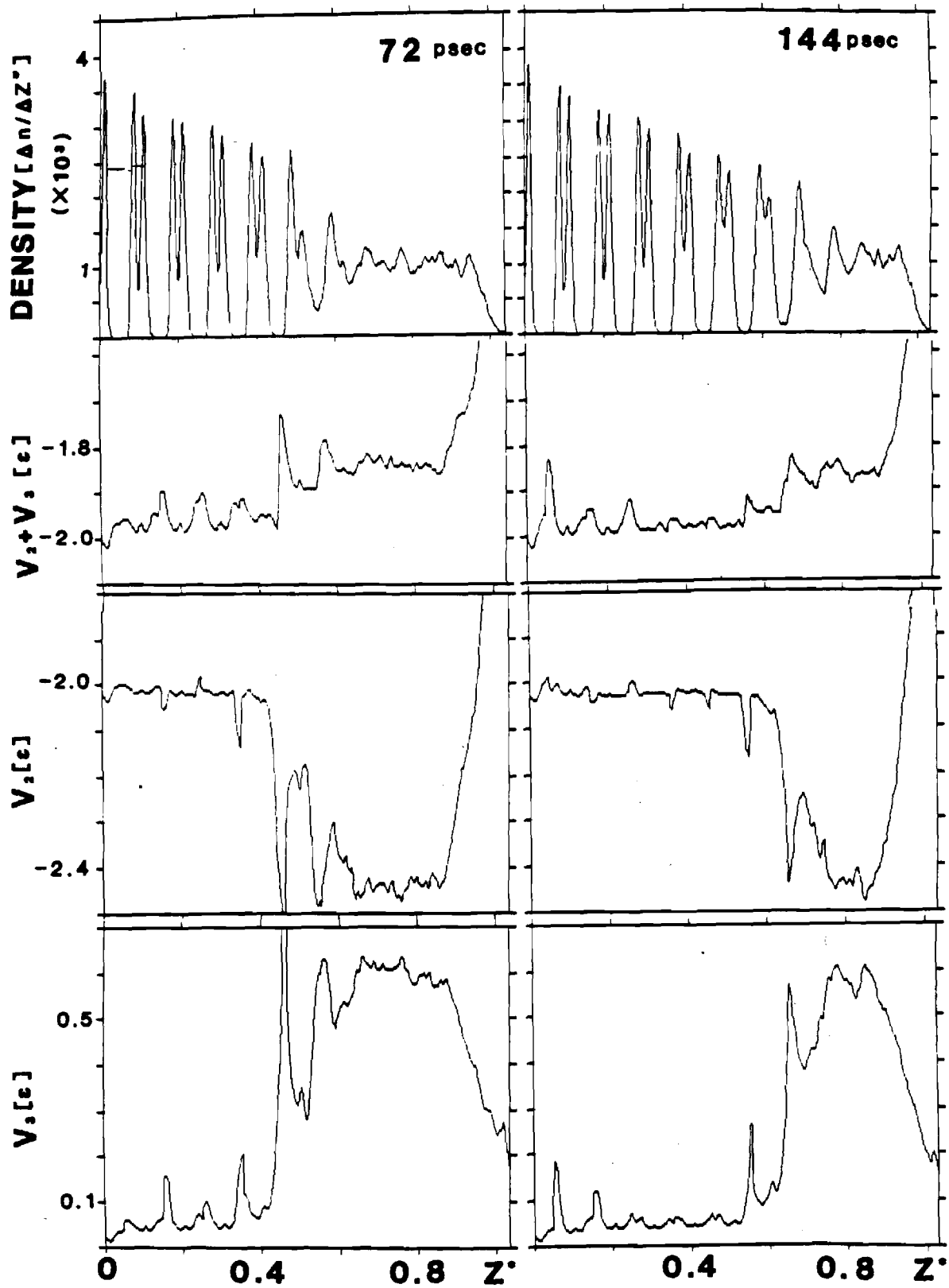


FIGURE 13

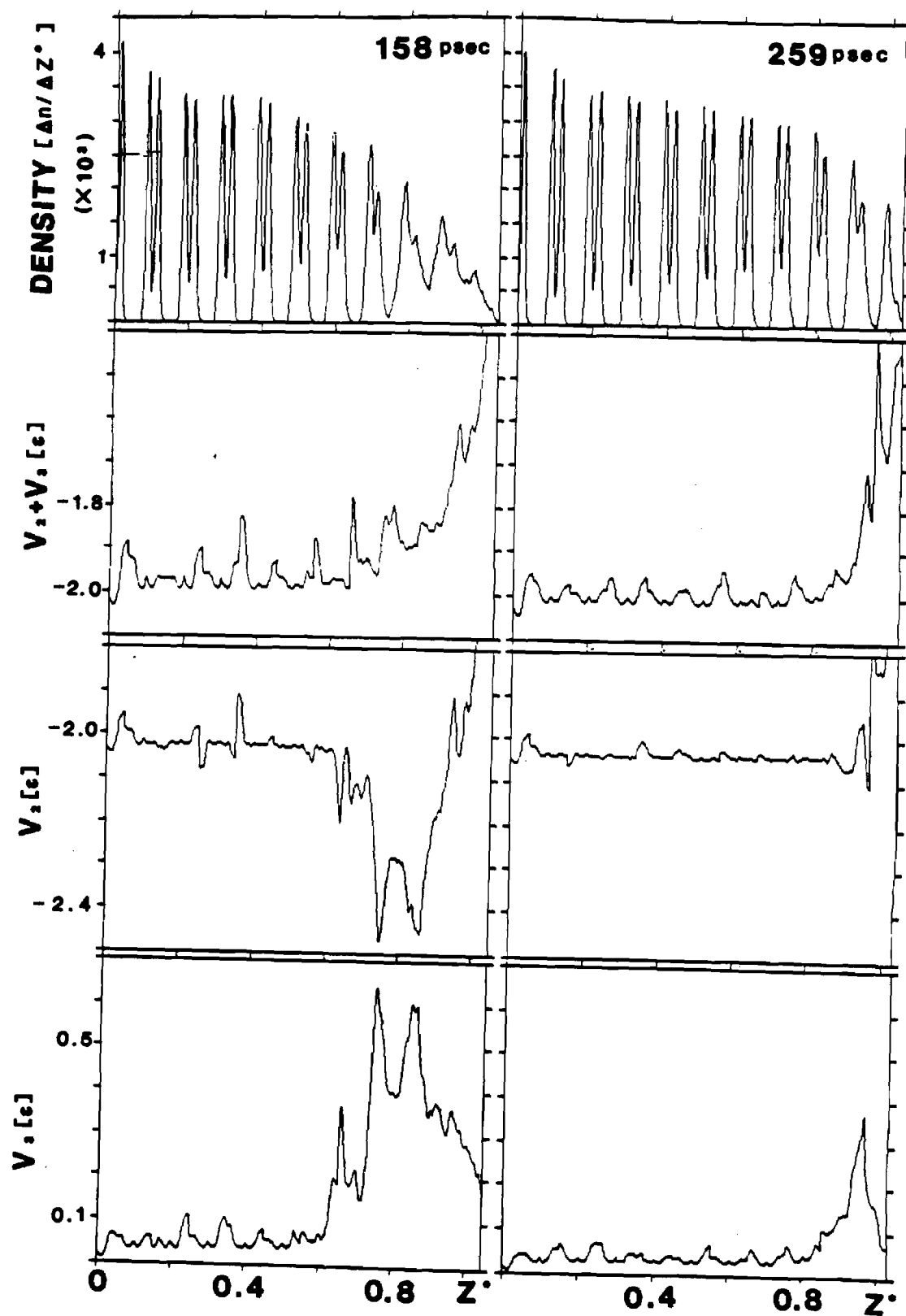


FIGURE 14

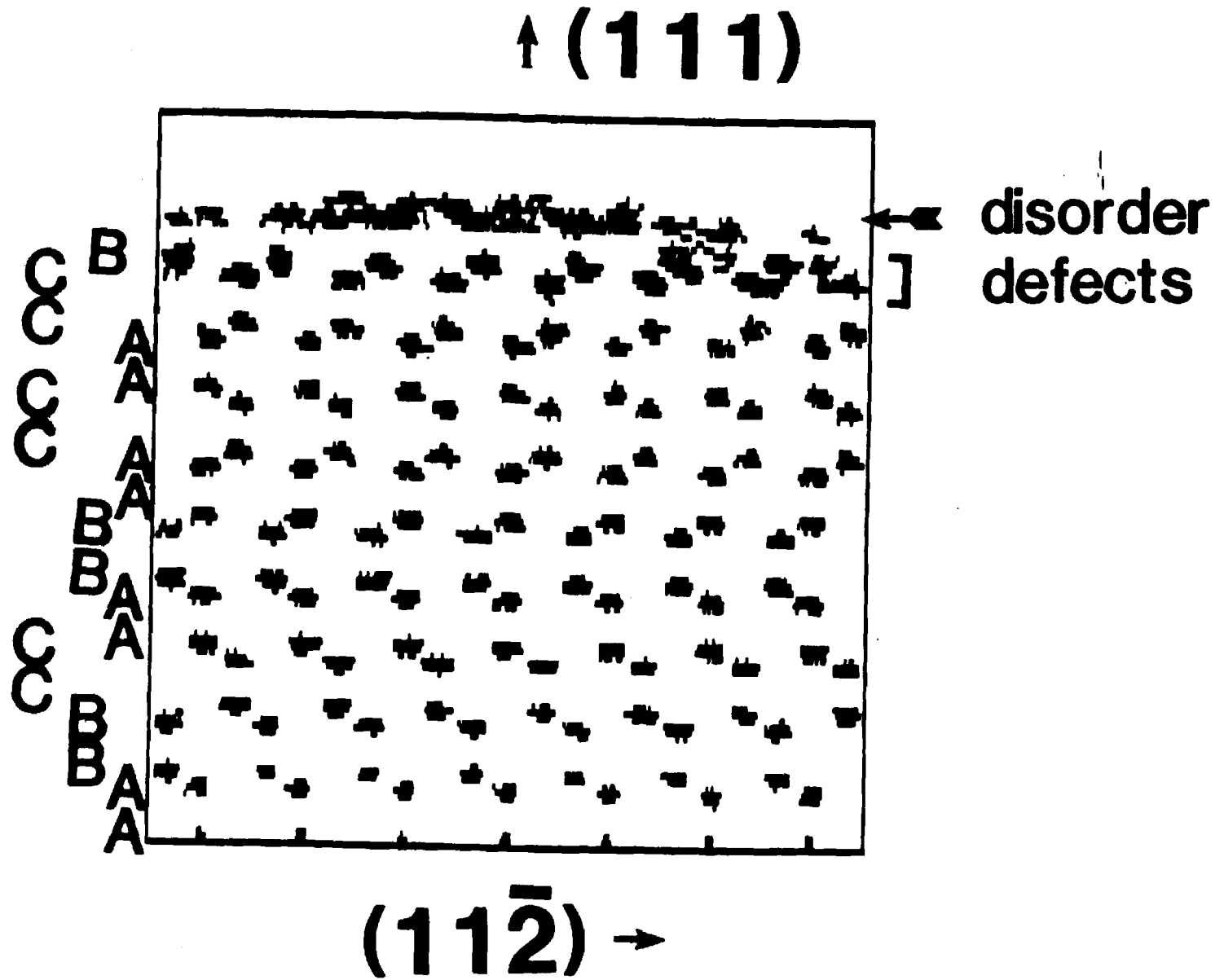


FIGURE 15